

# Global atmospheric hydrogen chemistry and long-term source-sink budget equilibrium simulation with the EMAC v2.55 model

Nic Surawski<sup>1,2</sup>, Benedikt Steil<sup>2</sup>, Christoph Brühl<sup>2</sup>, Sergey Gromov<sup>2</sup>, Klaus Klingmüller<sup>2</sup>, Anna Martin<sup>2</sup>, Andrea Pozzer<sup>2,3</sup>, and Jos Lelieveld<sup>2,3</sup>

<sup>1</sup>Centre for Green Technology, University of Technology Sydney, Gadigal Country, Ultimo NSW 2007, Australia

<sup>2</sup>Atmospheric Chemistry Department, Max Planck Institute for Chemistry, 55128 Mainz, Germany

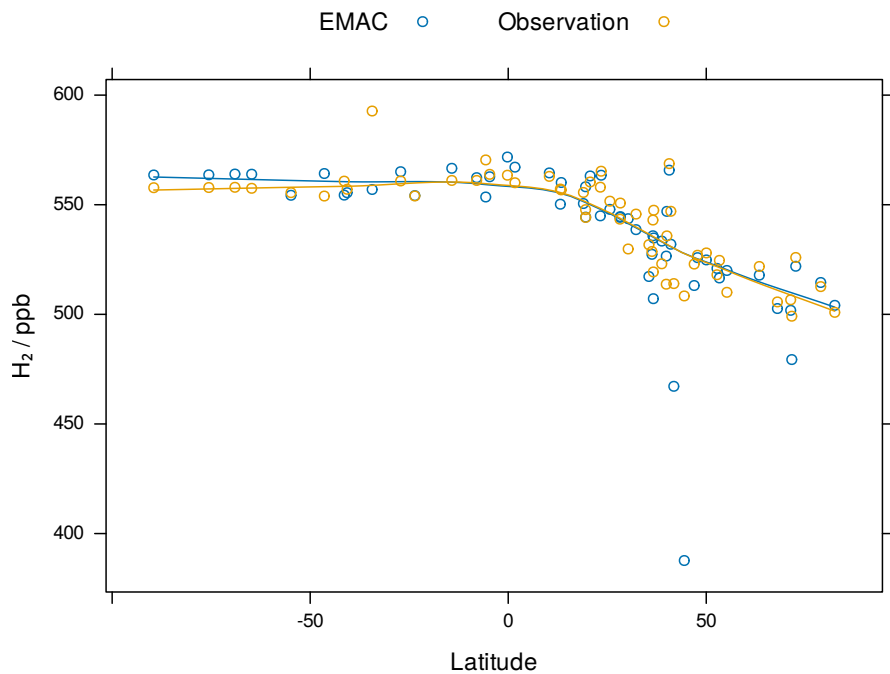
<sup>3</sup>Climate and Atmosphere Research Center, The Cyprus Institute, Nicosia, Cyprus

**Correspondence:** Nic Surawski (Nicholas.Surawski@uts.edu.au)

## Abstract

In this study, we use an earth system model with detailed atmospheric chemistry (EMAC v2.55.2) to undertake simulations of hydrogen ( $H_2$ ) atmospheric dynamics. Long-term global equilibrium simulations were performed with a horizontal resolution of 1.9 degrees. The results of this simulation are compared with long-term observational data from 56 stations in the National

5 Oceanic and Atmospheric Administration (NOAA) Global Monitoring Laboratory (GML) Carbon Cycle Cooperative Global Air Sampling Network. We introduced  $H_2$  sources and sinks, the latter inclusive of a soil uptake scheme, that accounts for bacterial consumption. The model thus accounts for detailed  $H_2$  and methane ( $CH_4$ ) flux boundary conditions. Results from the EMAC model are accurate and predict the magnitude, amplitude and interhemispheric seasonality of the annual  $H_2$  cycle at most observational stations. Time series comparison of EMAC and observational data produces Pearson correlation coefficients  
10 in excess of 0.9 at eight stations that experience well-mixed unpolluted air masses. A further 23 stations yielded correlation coefficients between 0.7–0.9 in remote tropical or mid-latitude locations. The quality of model predictions is reduced in anthropogenically highly polluted stations in east Asia and the Mediterranean region and stations impacted by peat fire emissions in Indonesia, as local and incidental emissions are difficult to capture. Our  $H_2$  budget corroborates bottom-up estimates in the literature in terms of source and sink strengths and overall atmospheric burden. By simulating hydroxyl radicals (OH) in the  
15 atmosphere leading to a  $CH_4$  lifetime in agreement with observationally constrained estimates, we show that the EMAC model is a capable tool for undertaking high accuracy simulation of  $H_2$  at global scale. Future research applications could target the impact of potentially significant natural and anthropogenic  $H_2$  sources on air quality and climate, reducing uncertainties in the  $H_2$  soil sink and impacts of  $H_2$  release on the future oxidising capacity of the atmosphere.



## Key figure

20 **1 Introduction**

H<sub>2</sub> represents an essential energy vector for 2050 net zero decarbonisation targets to be met. Current demand for H<sub>2</sub> equates to approximately 95 Mt per year with existing uses in the refining industry, as well as the chemical industry for production of ammonia, methanol and other chemicals (Hydrogen Council, 2021; International Energy Agency, 2023). H<sub>2</sub> is also used in the direct reduction of iron along with smaller uses in electronics, glassmaking and metal processing (International Energy Agency, 2023). With increased governmental, financial and policy support, demand for H<sub>2</sub> is forecasted to rise to between 430–690 Mt by 2050 (Hydrogen Council, 2021; International Energy Agency, 2023). Achieving this projected level of hydrogen demand can support clean energy use in: 1) hard to abate sectors such as long-haul trucking, shipping and aviation, 2) sectors that require a clean molecule as a chemical feedstock such as for co-firing of natural gas turbines or industrial processes such as steel manufacturing, 3) sectors that require a source of low carbon heat such as for cement and aluminium production or for buildings (Hydrogen Council, 2021; International Energy Agency, 2023). Use of H<sub>2</sub> offers a lot of potential for securing decarbonisation outcomes, provided clean production pathways are prioritised (Hydrogen Council, 2021; International Energy Agency, 2023), carbon capture and storage technologies (if required) work efficiently and at scale (International Energy Agency, 2020), and leakage rates in the H<sub>2</sub> value chain are minimised with sound engineering design (Esquivel-Elizondo et al., 2023; Fan et al., 2022).

35 Despite these potential advantages for decarbonisation, H<sub>2</sub> has well-documented climate impacts following its release into the atmosphere which represents an important environmental challenge. In terms of climate impacts, H<sub>2</sub> is an indirect greenhouse gas that leads to increases in radiatively active species by increasing 1) CH<sub>4</sub> lifetime due to H<sub>2</sub> competing for the OH sink 2) tropospheric ozone production due to a chain of reactions initiated by the H atom and 3) stratospheric water vapour that enhances radiative forcing (Derwent et al., 2006; Paulot et al., 2021; Ocko and Hamburg, 2022; Warwick et al., 2022, 2023).  
40 Since H<sub>2</sub> release affects the oxidising capacity of the atmosphere, it may also lead to changes in the production of sulphate, nitrate and secondary organic aerosols (Sand et al., 2023). Arising from these modelled results, coupled chemistry-climate modelling has a vital role to play before future H<sub>2</sub> infrastructure is installed to ensure that projected increases in H<sub>2</sub> utilisation do not lead to significant adverse consequences for the earth's atmosphere, air quality and climate.

50 Simulation of H<sub>2</sub> atmospheric chemistry impacts has attracted significant research attention both in the past few decades (Hauglustaine and Ehhalt, 2002; Schultz et al., 2003; Tromp et al., 2003; Warwick et al., 2004) and at present (Derwent et al., 2020; Paulot et al., 2021, 2024; Warwick et al., 2023) given the likelihood that demand for H<sub>2</sub> usage will grow and potential environmental impacts still require a solution. Previous attempts at simulating hydrogen mixing ratios with coupled chemistry-climate modelling have met variable levels of success at global scale. In this article, we show that the EMAC model is a highly capable tool for capturing 1) the magnitude, amplitude and seasonality of the annual H<sub>2</sub> cycle and 2) the meridional gradients in H<sub>2</sub> mixing ratios. These findings support the conclusion that the EMAC model consistently represents the interplay between the dominating soil sink (i.e. 75% of all sink terms) and atmospheric photochemical production (i.e. 63% of all source terms) which is by far the largest source term for H<sub>2</sub> (Table 2).

## 2 Materials and methods

In this work, we employ the EMAC model which couples the 5th generation European Centre Hamburg General Circulation Model (ECHAM5; Roeckner et al. (2003, 2004, 2006)) to the Modular Earth Submodel System (MESSy) (Jöckel et al., 2006, 2010). Simulations were performed with T63 spectral resolution which produces a spatial resolution of  $1.9^\circ$  (approximately 180–190 km). Simulations were performed with 90 levels up to 80 km above the earth’s surface, encompassing both the lower and middle atmosphere. Chemical reactions in the atmosphere were modelled with version 1 of the Mainz Isoprene Mechanism (MIM1; Pöschl et al. (2000); Jöckel et al. (2006)). The model experiment covers the time period 2006–2023, with the first three years used as spin-up time. Flux boundary conditions were employed for both  $\text{CH}_4$  and  $\text{H}_2$  to overcome issues with the introduction of artificial sources and sinks arising from using Dirichlet boundary conditions with a prescribed mixing ratio at the lower boundary of the atmosphere.  $\text{H}_2$  and  $\text{CH}_4$  are chemically coupled and have nearly the same chemical lifetime (Table 1). Both compete for the OH radical as a chemical sink, with OH being by far the dominant sink for atmospheric  $\text{CH}_4$  ((Saunois et al., 2025); see section 4.1 below). Furthermore, atmospheric oxidation of  $\text{CH}_4$  is the largest source for  $\text{H}_2$  (Ehhalt and Rohrer, 2009). To adequately simulate such a coupled system, the EMAC model uses flux boundary conditions for sources and sinks of both species. To reach a steady-state for the control simulation, the initial conditions for  $\text{CH}_4$  and  $\text{H}_2$  were obtained from a 15 years long simulation, covering the period 1990–2005.  $\text{CH}_4$  was simulated based on the work of Zimmermann et al. (2020), in which emissions of  $\text{CH}_4$  and deposition are represented based on the year 2020. Integration of the equations in the simulation uses a time-step of 450 seconds, and, due to the relatively long lifetime of  $\text{H}_2$ , precluding diel variability, instantaneous values are outputted every day.

### 2.1 Emissions

In this work, the goal is to undertake an equilibrium simulation that reaches steady-state mixing ratios representative of present day atmospheric conditions. Therefore, emissions are based on the year 2020, or the closest year prior to 2020, and are repeated for each year which removes any interannual variability. Due to increasing emissions and its long lifetime  $\text{CH}_4$  is not in a steady state. Therefore an equilibrium simulation is not fully representative of the atmospheric state in 2020.

For the long-lived tracer  $\text{CH}_4$ , the a posteriori emissions and the best combination of the rising- $\text{CH}_4$  scenario of Zimmermann et al. (2020) have been applied. In this work, Zimmermann et al. (2020) show that the EMAC model has been efficient in simulating interactive  $\text{CH}_4$  mixing ratios over the last two decades. Therein, the model results compare quite well with NOAA and The Advanced Global Atmospheric Gases Experiment (AGAGE) stations and measurements from CARIBIC (Civil Aircraft for the Regular Investigation of the atmosphere Based on an Instrument Container) flight observations (Brenninkmeijer et al., 2007). Twelve emission categories are considered here, namely, wetlands other than bogs (SWA), animals (ANI), landfills (LAN), rice paddies (RIC), gas production (GAS), shale gas drilling (SHA), bogs (BOG), coal mining (COA), including minor natural sources from oceans, other anthropogenic sources, volcanoes, oil production and offshore traffic, oil-related emissions (OIL), biomass burning (BIB), termites (TER), and biofuel combustion (BFC). Only emissions from bogs, rice fields, wetlands other than bogs, and biomass burning are subject to seasonal variability. Most of the emissions are based on the emission

fields of the Global Atmospheric Methane Synthesis (GAMeS) in which processes with similar isotopic characteristics are aggregated into one group (Houweling et al., 1999). For biomass burning, the GAMeS dataset is replaced by the GFEDv4s (Randerson et al., 2017) and is vertically distributed according to a profile suggested in the EDGAR database (Van Aardenne et al., 2005). The GFEDv4s biomass burning statistics include agricultural waste burning events. A total amount of 601.1 Tg 90  $\text{yr}^{-1}$  of  $\text{CH}_4$  is emitted in the model and detailed emissions for each sector can be found in Table 1 and 3 of Zimmermann et al. (2020), which also describe in detail the emission optimisation process.

$\text{H}_2$  emissions were taken from the RETRO dataset (Schultz et al., 2008), which was chosen due to its completeness. As for the other sources, we repeated the emissions based on one single year, namely the year 2000. The RETRO database covers the period 1960–2000, and the last year was taken as representative of 2020 emissions, motivated by the stagnation of  $\text{H}_2$  95 emissions in the past few decades (Paulot et al., 2021). A global value of 14.3 Tg  $\text{yr}^{-1}$  for anthropogenic emissions is obtained from the RETRO database, as well as 4.8 Tg  $\text{yr}^{-1}$  from soil emissions. Biomass burning emissions were obtained from the GFED (Global Fire Emissions Database) database (Giglio et al., 2013), and accounted for 8.35 Tg  $\text{yr}^{-1}$ . As the RETRO oceanic 100 emissions are outside the range of emissions suggested by the literature (Paulot et al., 2024), these emissions were upscaled to 3 Tg  $\text{yr}^{-1}$  so to be within the suggested range (i.e. between 3 – 6 Tg  $\text{yr}^{-1}$ ). Both the RETRO and GFED databases provide direct estimates of  $\text{H}_2$  emissions without relying upon an assumed  $\text{H}_2/\text{CO}$  emissions ratio.

For non-GHGs, different emissions were adopted. Anthropogenic sources of short-lived gases are based on CAMS-GLOB-ANTv4.2 and CAMS-GLOB-AIRv1.1 (Granier et al., 2019), and the emissions are estimated with reduction due to lockdowns during the COVID-19 pandemic (Reifenberg et al., 2022). The reduction in the mixing ratio of the OH radical is below 4% 105 for most of the atmosphere, with the exception of the uppermost troposphere and tropopause region, which is due to reduced flight activity. The small impact on OH is foremost confined to northern hemisphere mid-latitudes. Biomass burning emissions are calculated online on a daily basis and rely on dry matter burned from observations and fire type (Kaiser et al., 2012). The emission factors for different tracers and fire types are taken from Andreae (2019) and Akagi et al. (2011). The simulation uses a climatology of the aerosol wet surface density to calculate heterogeneous reactions. It is based on the CMIP5 (Climate Model Intercomparison Project Phase 5) emissions climatology for the years 1996–2005 low S scenario (Righi et al., 2013). 110 The aerosol distribution for radiative forcing calculation is the Tanre climatology (Jöckel et al., 2006). The biogenic emissions of organic species have been compiled following Guenther et al. (1995) and are prescribed in the model in an offline manner (Kerkweg et al., 2006), with the exception of biogenic isoprene and terpenes, for which the emissions are calculated online (Kerkweg et al., 2006).

## 2.2 Soil sink implementation

115 We estimate the soil sink using a two-layer soil model (Yonemura et al., 2000; Ehhalt and Rohrer, 2013a; Paulot et al., 2021).  $\text{H}_2$  is assumed to diffuse through a dry top layer of soil with no bacterial activity (layer I), which may be covered by an equally inactive layer of snow. In a second layer below the top layer (layer II), the rate of  $\text{H}_2$  removal by high-affinity hydrogen-oxidising bacteria (Paulot et al., 2021) depends on both soil temperature and moisture. The resulting deposition rate is parameterised by:

$$v_d = \frac{1}{(\delta/D_{\text{soil}}(\theta_w, \text{I}) + \delta_{\text{snow}}/D_{\text{snow}} + 1/\sqrt{(D_{\text{soil}}(\theta_w, \text{II}) A g(T) f(\theta_w, \text{II}/\theta_p))})} . \quad (1)$$

120

The first two terms in parenthesis in the denominator of Eq. (1) represent diffusion through the inactive soil layer and the snow layer of thickness  $\delta$  and  $\delta_{\text{snow}}$ , respectively. The diffusivity of  $\text{H}_2$  in soil is given by Millington and Quirk (1959):

$$D_{\text{soil}}(\theta_w) = ((\theta_p - \theta_w)^{3.1}/\theta_p^2) D_{\text{air}}, \quad (2)$$

which depends on the volumetric soil water fraction  $\theta_w$  and the volumetric soil pore fraction (i.e. porosity)  $\theta_p$ . The diffusivity 125 of  $\text{H}_2$  in snow is given by:

$$D_{\text{snow}} = 0.64 D_{\text{air}}, \quad (3)$$

while the diffusivity of  $\text{H}_2$  in air is given by:

$$D_{\text{air}} = 0.611 \frac{((T + 273.15)/273.15)^{1.75}}{p/1013.25}, \quad (4)$$

where the diffusivity of  $\text{H}_2$  in air depends on the air temperature  $T$  in  $^{\circ}\text{C}$  and the air pressure  $p$  in hPa.

130 The third term in parenthesis in the denominator of Eq. (1) represents  $\text{H}_2$  removal in the lower, active layer. The temperature dependence is given by Ehhalt and Rohrer (2011):

$$g(T) = \frac{1}{(1 + \exp(-(T - 3.8)/6.7)} + \frac{1}{(1 + \exp((T - 62.2)/7.1)} - 1, \quad (5)$$

where  $T$  is the soil temperature in  $^{\circ}\text{C}$ .

135 The soil moisture dependence in terms of the water saturation  $S = \theta_w/\theta_p$  for eolian sand is given by Ehhalt and Rohrer (2011):

$$f_{\text{es}}(S) = 0.00936 \frac{(S - S_{\text{es}}^*)(1 - S)}{S^2 - 0.1715S + 0.03144}, \quad (6)$$

where  $S_{\text{es}}^* = 0.02640$  is the minimum level of water saturation required for microbial activity. For loess loam the soil moisture dependency is given by Ehhalt and Rohrer (2011):

$$f_{\text{ll}}(S) = 0.01997 \frac{(S - S_{\text{ll}}^*)(0.8508 - S)}{S^2 - 0.7541S + 0.2806}, \quad (7)$$

140 where  $S_{\text{ll}}^* = 0.05369$ . For a mixture of eolian sand and loess loam we use the weighted mean given by:

$$f(S) = \varphi_{\text{sand}} f_{\text{es}}(S) + (1 - \varphi_{\text{sand}}) f_{\text{ll}}(S), \quad (8)$$

where  $\varphi_{\text{sand}}$  is the sand fraction of the soil.

The resolution-dependent constant  $A$  represents bacterial activity and is adjusted to yield a global mean deposition velocity of

0.033 cm s<sup>-1</sup> over land during 2012 to 2015 (Yashiro et al., 2011). Using the 0.25° grid spacing of the ERA5 input data, we

145 obtain  $A = 10.9$ .

The thickness of the upper soil layer without hydrogenase (i.e. an enzyme in prokaryotes such as bacteria that consume H<sub>2</sub>) activity is parametrised by:

$$\delta_s = 0.0057((\theta_p - \theta_w)/\theta_w)^{2.5}, \quad (9)$$

in sandy loam and

$$150 \quad \delta_l = 0.109((\theta_p - \theta_w)/\theta_w)^{1.8}, \quad (10)$$

in loam. Both  $\delta_s$  and  $\delta_l$  are expressed in cm. For a mixture of sandy loam and loam with sand fraction  $\varphi_{\text{sand}}$  we use the weighted mean to calculate the soil layer thickness via:

$$\delta = \varphi_{\text{sand}}\delta_s + (1 - \varphi_{\text{sand}})\delta_l. \quad (11)$$

The soil water content in the top, dry layer (i.e.  $\theta_{wI}$ ) is assumed to be the threshold moisture content below which the bacterial

155 activity vanishes, i.e. there is no H<sub>2</sub> uptake in this layer, and is given by:

$$\theta_{wI} = S^* \theta_p, \quad (12)$$

where  $S^* = S_{\text{es}}^*$  is the threshold moisture content for eolian sand and  $S^* = S_{\text{ll}}^*$  for loess loam.

Accordingly, the remaining water within the top 10 cm of soil is between depth  $\delta$  and 10 cm, resulting in a soil water content for the second layer (i.e.  $\theta_{wII}$ ) of:

$$160 \quad \theta_{wII} = \frac{10\theta_w - \delta\theta_{wI}}{10 - \delta}. \quad (13)$$

We evaluated Eq. (1) using monthly reanalysis data for soil moisture, soil temperature, air pressure, snow depth and snow density with a 0.25° grid spacing from the ERA5 dataset provided by the European Centre for Medium-Range Weather Forecasts (ECMWF) (Hersbach et al., 2020, 2023). The mean soil moisture and soil temperature for the top 10 cm soil layer was

165 obtained by linearly interpolating the ERA5 soil level data. The volumetric soil water content was then uniformly reduced by 6% (Paulot et al., 2021). Static soil porosity and sand fraction maps with 0.25° grid spacing were obtained from the Land Data

## 2.3 Observations

EMAC simulations are compared with observational data from 56 stations (with more than 12 monthly values) that form part of the NOAA GML Carbon Cycle Cooperative Global Air Sampling Network (Petron et al., 2024). Data gaps exist at some

170 stations due to the application of quality control procedures, as well as missing data due to impacts of the COVID-19 pandemic.

For comparison with the results of the EMAC equilibrium simulation, the observed monthly values have been detrended by subtracting the trend obtained by a sixth order harmonic regression with a linear trend term, while keeping the mid-year values

for 2020 fixed.

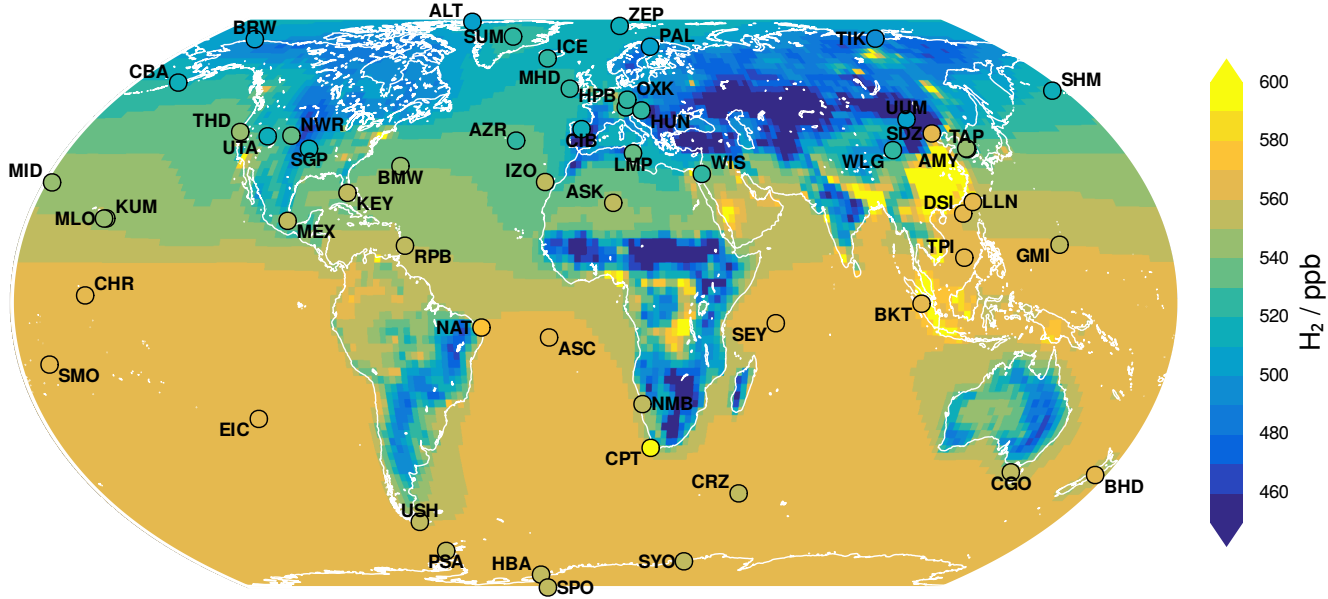


**Figure 1.** Global map of  $\text{H}_2$  mixing ratios and the location of observational stations. Model data is averaged over the years 2010–2023 (inclusive) which is representative of the year 2020 for a steady-state simulation, while observational data uses mid-2020 values from a detrending fit using a sixth order harmonic regression technique.

### 3 Results

175 Figure 1 presents a global map of modelled annual mean  $\text{H}_2$  mixing ratios as well as the location of observational stations that we use for model inter-comparison purposes. This global map shows the inter-hemispheric gradient for this molecule whereby  $\text{H}_2$  mixing ratios are higher in the southern hemisphere compared to the northern hemisphere. This global map also shows the influence of pollution hotspots in Asia, and the influence of biomass burning emissions in central Africa and peat fire emissions in southeast Asia.

180 We show time series data for model comparisons with observational data (without gaps in monthly data) from 20 observational stations in Fig. 2. Further comparisons with observational data from another 36 observational stations (with data gaps) are shown in Fig. B1 and B2. Across these 56 observational stations, the Pearson correlation coefficient ( $r$ ) exceeds 0.9 for eight stations that experience well-mixed unpolluted air masses. Such stations are either remote or located at high latitude in either the Arctic or Antarctic regions. In such cases, the annual cycle of  $\text{H}_2$  is modelled excellently in terms of magnitude, 185 amplitude and seasonality. In contrast, the three stations in the Mediterranean region; namely, Lampedusa (LMP, 0.04), CIBA in northern central Spain (CIB, -0.17) and Israel (WIS, -0.29) produce correlation coefficients close to zero or even negative. The same holds for two stations located in Shangdianzi (China, SDZ, -0.2) and Ulaan Uul (Mongolia, UUM, 0.03). The EMAC model is under-performing at two tropical coastal stations, Natal (Brazil, NAT) and Bukit (Indonesia, BKT) with correlation coefficients of 0.14 in contrast to other tropical stations. These stations are located in regions that do not experience well-mixed

190 unpolluted air masses (e.g. Mediterranean region, UUM, SDZ) or are impacted by biomass burning (i.e. NAT) and peat fire emissions (i.e. BKT). Negative  $r$  values suggest that the EMAC model does not correctly capture the phasing of the annual H<sub>2</sub> cycle which results in an anti-correlation in Table B1. Another 23 stations have correlation coefficients between 0.7–0.9 which demonstrate very good agreement between model and observational data. A number of these stations are located in the 195 mid-latitudes either in the northern or southern hemisphere. The remaining 18 stations produce correlation coefficients between 0.3–0.7 mostly in either remote tropical or mid-latitude regions. Especially the Antarctic stations show an upward trend for atmospheric H<sub>2</sub>. The model with its emissions and soil sink repeating the year 2020, cannot capture this feature. This trend coincides with further increasing atmospheric CH<sub>4</sub> concentrations after 2010 following its hiatus of the previous decade (Lan et al., 2024). Table 2 shows that oxidation of atmospheric CH<sub>4</sub> is the largest source term for H<sub>2</sub> Ehhalt and Rohrer (2009). To 200 investigate this further in the future, a model simulation with flux boundary conditions for H<sub>2</sub> and CH<sub>4</sub> in transient mode is needed. Overall, the results are very promising and demonstrate the ability of the EMAC model to predict H<sub>2</sub> mixing ratios accurately in most regions of the earth. To provide a visual overview of these results, Fig. 3 provides a global map of Pearson correlation coefficients for comparison of EMAC and observational data.

We also present a plot of the meridional gradient in H<sub>2</sub> in Fig. 4. Overall, meridional gradients in H<sub>2</sub> are captured very well by the EMAC model, notably for stations located in the southern hemisphere, likely because many represent the background 205 atmosphere, whereas many stations in the northern hemisphere are affected by local influences. The model correctly predicts higher H<sub>2</sub> mixing ratios in the southern hemisphere even though the majority of H<sub>2</sub> sources are present in the northern hemisphere. The predicted interhemispheric gradient in H<sub>2</sub> presented here is correct by virtue of the greater soil sink that is present in the northern hemisphere arising from its larger land area (Ehhalt and Rohrer, 2009). Most of the discrepancies between the 210 observed and predicted H<sub>2</sub> mixing ratios exist for a small number of stations within the northern hemisphere mid-latitudes (between 30–60° N) and in the tropics, presumably influenced by local source variability that is insufficiently resolved by our global model. The coverage of many continental land masses by the observational stations is sparse. For South America, Australia, Africa, Central Asia, Siberia and India there are almost no measurements available. This is a problem, especially in validating the soil sink, which can be considered the most uncertain part of the H<sub>2</sub> budget (Paulot et al., 2021).

For further results, we refer the reader to Appendix B which provides further graphs and tabulated summaries of model 215 performance.

## 4 Discussion

### 4.1 Model comparison with observational data

A key feature of the results (Fig. 2, Fig. B1 and Fig. B2) is the ability of the EMAC model to realistically predict the magnitude, 220 amplitude and seasonality of the annual H<sub>2</sub> cycle at most stations, in unison with that from CH<sub>4</sub> Zimmermann et al. (2020), with both compounds being modelled with flux boundary conditions and interactive sinks. Promising results are obtained especially for stations that experience well-mixed unpolluted air masses, for example, in mostly polar regions, which are particularly sensitive to atmospheric transport and chemistry dynamics. The EMAC model results are also quite promising in a range of

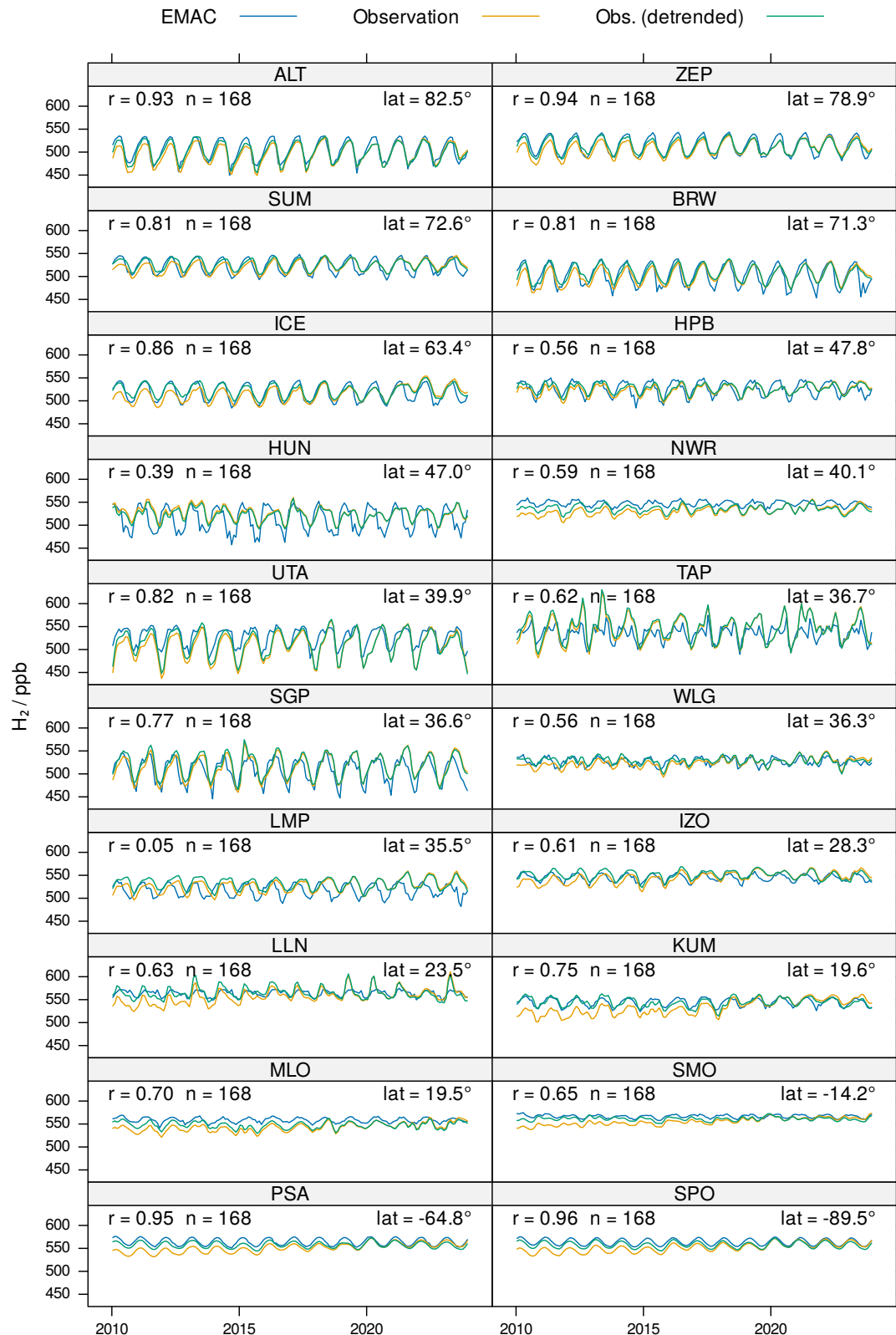


**Figure 2.** Time series comparison of observational and EMAC model data for H<sub>2</sub>. Results are presented for 20 stations without any gap in monthly data. The sample size for observational data is denoted by  $n$ , while  $r$  is the Pearson correlation coefficient. Latitudes are denoted by  $lat$ .

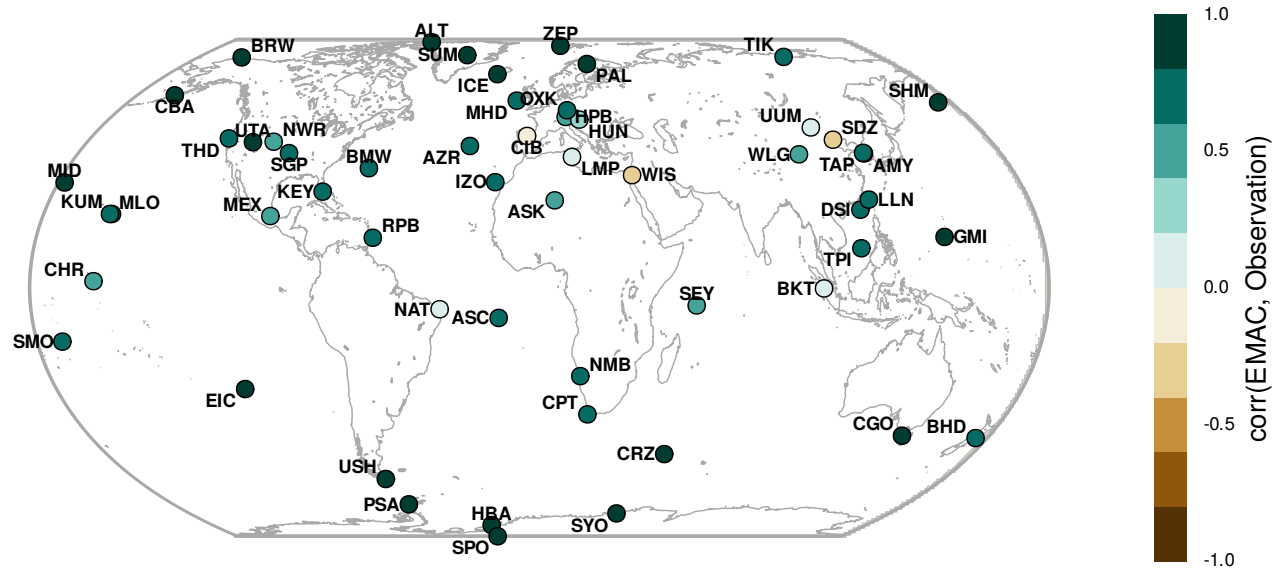


**Figure 3.** Pearson correlation coefficient for the intercomparison between EMAC and observational data for H<sub>2</sub>. Model data is compared with detrended observational data for the years 2010–2023 (inclusive) to perform this calculation.

mid-latitude stations both in the northern and southern hemisphere. In contrast, there are some regions of the globe (Fig. 3) where results are not as promising. For example, the EMAC model predictions are less accurate in the highly anthropogenically 225 polluted Mediterranean region, near the Amazonian region which is impacted by biomass burning emissions, and southeast Asia which is impacted by peat fire emissions. Due to the coarse spatial resolution of 180–190 km and limited information about local and incidental sources, the variability of mixing ratios in these regions is more challenging to capture. This is especially the case for some coastal stations (e.g. NAT, BKT) where the model is limited due to resolution in accurately 230 representing the mixing of marine and continental air. Also the deviations in China and Mongolia (SDZ, UUM) can be partly attributed to a resolution effect. Both stations are located close to strong horizontal gradients in H<sub>2</sub> mixing ratios. The vertical 235 resolution of the lowermost model layers (i.e. thicknesses of 66 m, 166 m and 319 m from the surface upwards) and the representation of the orography influence the comparison. It is important to consider the measurement height relative to the surface and the geographic prominence of the stations. For example, the modelled amplitude of the annual H<sub>2</sub> cycle can be reduced by up to 40% between the surface and the next model layer for continental stations due to the importance of the 240 soil sink, whereas the H<sub>2</sub> mixing ratios increase with height driven by the strong atmospheric chemical H<sub>2</sub> production. In addition, an interesting model-measurement discrepancy occurs at the Weizmann Institute of Science (WIS) station near the 245 northern Red Sea, where unaccounted for alkane emissions have been attributed to natural seepage from deep water sources (Bourtsoukidis et al., 2020), possibly accompanied by H<sub>2</sub> emissions. Overall, the EMAC model performs favourably at a global

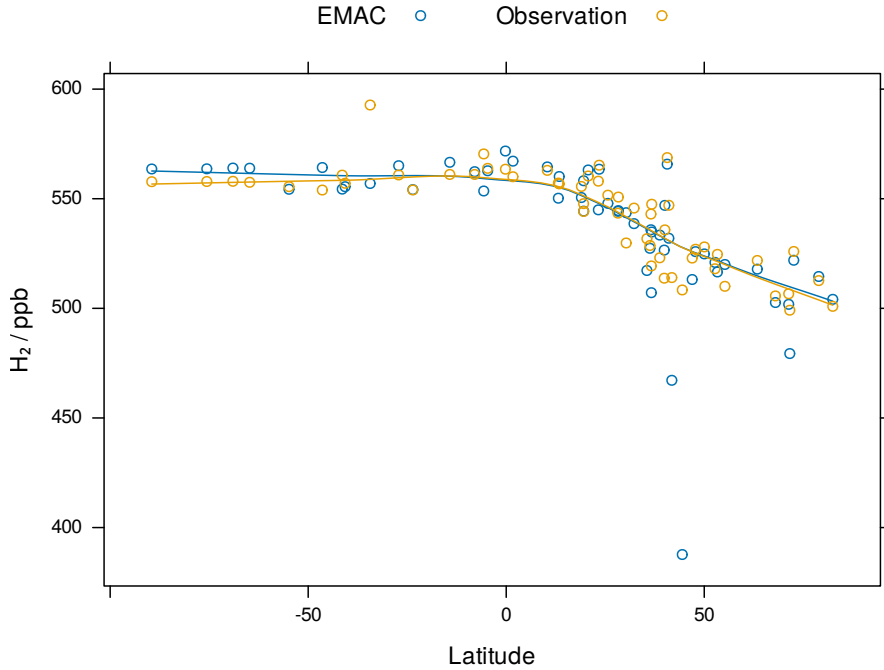


**Figure 4.** Meridional gradients in  $\text{H}_2$  for EMAC predictions and observational data where stations had more than 12 monthly values. The solid lines were obtained by locally estimated scatterplot smoothing (LOESS; smoothing parameter 2 / 3, locally linear). Negative latitudes represent south and positive latitudes represent north of the equator. Data are shown for stations with more than 12 monthly values.

scale for simulating  $\text{H}_2$  mixing ratios. Comparison with model output from Yashiro et al. (2011) shows that while the EMAC 240 model produces correlation coefficients in excess of 0.7 for over half of the observational stations, the CHASER chemistry-climate model achieves the same result for only one quarter of all observational stations. The annual mean  $\text{H}_2$  mixing ratios are well captured by the EMAC model (Table B1 and Fig. 4), with the exception of CIB ( $r=-0.17$ ), UUM ( $r=0.03$ ), and the coastal station Cape Town (CPT) despite its high Pearson correlation coefficient ( $r=0.73$ ).

To successfully simulate  $\text{H}_2$  mixing ratios in the atmosphere, a model needs to correctly resolve the complex interplay between meteorology and chemistry. In terms of chemistry, having the oxidising capacity of the atmosphere represented correctly is a key consideration (Prather and Zhu, 2024). It is largely controlled by the concentration of OH radicals in the troposphere (Lelieveld et al., 2016) and determines the atmospheric lifetime of numerous species including  $\text{CH}_4$ . The total  $\text{CH}_4$  sink is largely dominated by its reaction with OH (see Saunois et al. (2025) for a review). In this sense,  $\text{CH}_4$  lifetime is a measure for the total oxidative capacity of the atmosphere. Observational estimates derived from methyl chloroform ( $\text{CH}_3\text{CCl}_3$ ) measurements lead to a total atmospheric  $\text{CH}_4$  lifetime of  $9.1 \pm 0.9$  years (Prather et al., 2012). Our estimate of  $9.3 \pm 0.06$  years (Table 1) compares well, and is only marginally higher than the range indicated by Prather et al. (2012). This also holds for the global tropospheric chemical  $\text{CH}_4$  sink. The supporting information of Prather et al. (2012) states that for the tropospheric  $\text{CH}_4$  lifetime based on the reaction with OH (i.e.  $11.2 \pm 1.3$  years) and for the lifetime of  $\text{CH}_4$  based on the reaction with tro- 250

pospheric chlorine (i.e.  $200 \pm 100$  years) yields a combined tropospheric chemical lifetime of  $10.6 \pm 1.2$  years for  $\text{CH}_4$ . This  
255 value compares quite well with our estimate of 10.4 years (Table 1). Model intercomparisons performed by Nicely et al. (2020)  
suggests that many chemistry models underestimate  $\text{CH}_4$  lifetime due to simulating an atmosphere that is overly enriched in  
OH radicals. Recently, work by Yang et al. (2025) concurs that several atmospheric chemistry models over-predict OH mixing  
ratios which has implications for  $\text{CH}_4$  and  $\text{H}_2$  lifetimes. The multi-model estimate from CMIP6 (Coupled-Model Intercompar-  
ison Project 6; Collins et al. (2017)) and CCMCI (Chemistry Climate Model Initiative; Plummer et al. (2021)) models used by  
260 the Global Carbon Project community for the bottom-up estimates of  $\text{CH}_4$  sources yields a total  $\text{CH}_4$  lifetime of 8.2 years with  
a range of 6.8–9.7 years (Saunois et al., 2025). It also shows a large spread, which propagates into increased uncertainties for  
the derivation of emission budgets. We believe that the EMAC model is realistically capturing the total oxidising capacity of  
the atmosphere which helps to facilitate high-accuracy prediction of  $\text{H}_2$  and  $\text{CH}_4$  dynamics.

## 4.2 Budget and lifetimes

265 In the atmosphere,  $\text{CH}_4$  and  $\text{H}_2$  are tracers strongly connected with similar chemical fates. Table 1 shows that  $\text{CH}_4$  and  $\text{H}_2$   
have nearly identical chemical lifetimes both in the troposphere and atmosphere. Furthermore the total sources of  $\text{H}_2$  and  
 $\text{CH}_4$ , corrected for molecular masses, are very comparable. The biggest difference between these two compounds stems from  
hydrogen's much larger soil sink which reduces its tropospheric lifetime by approximately a factor of four compared to  $\text{CH}_4$ .

270 In Table 2, we compare our  $\text{H}_2$  budget derived from EMAC model output with other estimates from the literature. We find  
that our  $\text{H}_2$  budget agrees favourably with bottom-up literature estimates that rely on a combination of emission datasets and  
model calculations of turnovers and loss rates, but differs from top-down estimates relying on either inverse modelling (Xiao  
et al., 2007) or analysis of the  $^2\text{H}$  (i.e. deuterium) budget (Rhee et al., 2006). Our overall budgeting of sources and sinks  
agrees very well with bottom-up estimates. In addition, our tropospheric  $\text{H}_2$  lifetime is in very good agreement with bottom-up  
estimates. The tropospheric burden is in the upper range of model estimates. Note, that the upper boundary of the tropospheric  
275 range is often not clearly defined in the literature, with different definitions e.g. 100 hPa, World Meteorological Organization  
(WMO), or a climatological tropopause being used. In this study the WMO tropopause definition is used based on a dynamic  
tropopause in high latitudes and lapse rate being used at low latitudes. The photochemical production is in between the range  
for bottom-up and top-down estimates (Paulot et al., 2021). These findings suggest that the EMAC model simulates a realistic  
atmospheric oxidation capacity which is a critical requirement for predicting  $\text{H}_2$  mixing ratios well.

280 Recent work by the United States Geological Survey (Ellis and Gelman, 2024) has developed a simple, zero-dimensional  
mass balance model coupled with Monte Carlo uncertainty analysis to explore global potential for geological (or gold)  $\text{H}_2$   
production in the earth's crust. Median modelled estimates of the subsurface  $\text{H}_2$  resource are approximately  $5.6 \times 10^6$  mega-  
tonnes. Ellis and Gelman (2024) estimate that global geological  $\text{H}_2$  resources cause an additional global flux of  $24 \text{ Tg yr}^{-1}$   
from the subsurface to the atmosphere. This is speculative and would add unaccounted  $\text{H}_2$  emissions almost of the strength  
285 of the current non-photochemical sources. Current knowledge concerning the budget of atmospheric  $\text{H}_2$  does not exclude the  
existence of a large geological  $\text{H}_2$  reservoir, and further emphasises the importance of dry deposition for the global atmospheric  
 $\text{H}_2$  budget.

**Table 1.** Chemical budgets and lifetimes for H<sub>2</sub> and CH<sub>4</sub>. Uncertainties are calculated as the standard deviation of multi-year annual global means. Note that lifetimes are always calculated with respect to global burden (Prather et al., 2012; SPARC, 2013).

Budget term	H <sub>2</sub>	CH <sub>4</sub>
Tropospheric chemical sink (Tg yr <sup>-1</sup> )	19.0 ± 0.16	534.5 ± 4.04
Tropospheric chemical production (Tg yr <sup>-1</sup> )	49.5 ± 0.43	-
Tropospheric chemical lifetime (years)	10.5 ± 0.08	10.4 ± 0.08
Atmospheric chemical lifetime (years)	9.6 ± 0.07	9.8 ± 0.07
Soil sink (Tg yr <sup>-1</sup> )	60.5 ± 0.07	30.9 ± 0.02
Tropospheric lifetime (years)	2.5 ± 0.004	9.9 ± 0.07
Atmospheric lifetime (years)	2.5 ± 0.004	9.3 ± 0.06

### 4.3 Suggestions for future applications

Future research efforts in modelling H<sub>2</sub> atmospheric chemistry could build on the current work in three key ways. Firstly, scenarios could be constructed to explore what role geological H<sub>2</sub> (i.e. gold H<sub>2</sub>) holds for future atmospheric chemistry. If economically extractable reserves of gold H<sub>2</sub> are found, future utilisation of H<sub>2</sub> would increase well beyond current projections (Hand, 2023; Truche et al., 2024; Ellis and Gelman, 2024). It would therefore be critical to assess the atmospheric chemistry implications of vastly increased H<sub>2</sub> usage. Secondly, it will be critical to assess what impact H<sub>2</sub> use has on the future oxidising capacity of the atmosphere. Clean H<sub>2</sub> use will be associated with significant reductions in the co-emission of criteria pollutants (Galimova et al., 2022) which will influence the formation of atmospheric oxidants such as ozone and OH radicals that constrain CH<sub>4</sub> and H<sub>2</sub> lifetimes (Archibald et al., 2011; Brasseur et al., 1998; Ganzeveld et al., 2010). Thirdly, the H<sub>2</sub> budget is dominated by the land sink (Tables 1 and 2) and future research efforts could help to constrain the important role played by a number of soil properties (e.g. porosity, soil moisture, temperature, and organic carbon content) on terrestrial H<sub>2</sub> uptake (Ehhalt and Rohrer, 2011, 2013a; Paulot et al., 2021; Smith-Downey et al., 2006). The production of H<sub>2</sub> by enzymes in soil (i.e. hydrogenases) could also be considered in a depth-resolved manner as knowledge of the underlying processes improves (Ehhalt and Rohrer, 2013b). Recent coupling of the JSBACH vegetation model to EMAC by Martin et al. (2024) has developed a potential model tool for undertaking on-line H<sub>2</sub> land sink calculations.

**Table 2.** Tabulation of the H<sub>2</sub> budget from this study and from literature estimates. Uncertainties are calculated as the standard deviation of multi-year annual means.

Budget term	This study (EMAC)	Seiler and Conrad (1987)	Warneck (1988)	Novelli et al. (1999)	Hauglustaine and Ehhalt (2002)	Sanderson et al. (2003)	Rhee et al. (2006)	Price et al. (2007)	Xiao et al. (2007)	Ehhalt and Rohrer (2009)	Pieterse et al. (2011)	Yashiro et al. (2011)	Paulot et al. (2021)	Sand et al. (2023) <sup>c</sup>	Paulot et al. (2024)
<b>Sources: Tg yr<sup>-1</sup></b>															
<b>Tropospheric</b>	79.1 ± 0.4	87 ± 38	89	77 ± 16	70	78.2	107 ± 11	73	76 ± 14	77.3	73–80	74.4	74–102	74 ± 1	
Photochemical	49.5 ± 0.4	40 ± 15	50	40 ± 16	31	30.2	64 ± 12	34.3	41 ± 11	37.3	38–39	42.1	34–56	44	
CH <sub>4</sub> oxidation	34.5 ± 0.4	15 ± 5	29	26 ± 9		15.2		24.5		23 ± 8				27	
VOC oxidation	15.0 ± 0.2	25 ± 10	21	14 ± 7		15		9.8		18 ± 7				17	
Direct	29.6	47	39	37	39	48	43	38.8	27	35	40	30–37	32.3	23–68	30
Ocean	3 <sup>a</sup>	4 ± 2	4	3 ± 2	5	4	6 ± 5	6 ± 3	6 ± 3	5	5	6	6	6	6
Biofuel								4.4							
Soil	4.8	3 ± 2	3	3 ± 1	5	4	6 ± 5	0	3 ± 2	3	3	3	3	3	3
Biomass															
burning	7.5	20 ± 10	15	16 ± 5	13	20	16 ± 3	10.1	12 ± 3	15 ± 6	15	8–15	9		8
Anthropogenic	14.3	20 ± 10	17	15 ± 10	16	20	15 ± 6	18.3	15 ± 10	11 ± 4	17	15.1–15.4	14.3		13
<b>Atmospheric</b>	81.1 ± 0.4								103 ± 10						
Photochemical	51.5 ± 0.4								76 ± 9						
Stratospheric CH <sub>4</sub> oxidation	1.94 ± 0.02														
Stratospheric VOC oxidation	0.08 ± 0.02														
<b>Sinks: Tg yr<sup>-1</sup></b>															
Troposphere	81.2 ± 0.2	98 ± 23	89	75 ± 41	70	75.4	107 ± 11	73	103.9	79	77.9	75–78	75.1	75–102	
Soil uptake	60.5 <sup>b</sup> ± 0.1	90 ± 20	78	56 ± 41	55	58.3	88 ± 11	55 ± 8.3	84 ± 8	60	55.8	57–60 ± 12	54.7	44–73	
Photochemical	20.8 ± 0.2	8 ± 3	11	19 ± 5	15	17.1	19 ± 3	18	19.9	19	22.1	17–18	20.4	22–30	
Troposphere	19.0 ± 0.2								18 ± 3						
Stratosphere	1.8 ± 0.01								1.9 ± 0.3						
<b>Burden: Tg</b>	199.6 ± 0.2								191 ± 29					184–209	
Stratosphere	34.4 ± 0.1								42						
Troposphere	165.2 ± 0.3	163	155 ± 10	136	172	150	141	149 ± 23	155 ± 10	169	148–153	157.4			
IHD (ppbv)	29.4 ± 0.4														
Lifetime (years)	2.1 ± 0.003		1.8	2.1	1.9	2.2	1.4	1.9	1.4 ± 0.2	2	2.2	1.9–2.0	2.1	1.9–2.7	2.5

<sup>a</sup> Up-scaled from 0.5 to 3 Tg/yr to match literature recommendations (Paulot et al., 2021); <sup>b</sup> the dry deposition velocity of H<sub>2</sub> Paulot et al. (2021) has been reduced by 6% (from the continental global mean of 0.035 to 0.033 cm s<sup>-1</sup> to improve simulated H<sub>2</sub> especially in polar latitudes. <sup>c</sup> Multi-model results are presented as a range. VOC = volatile organic compound. IHD = interhemispheric difference.

## 5 Conclusions

In this study, we have successfully extended and used the EMAC model to undertake simulations of H<sub>2</sub> atmospheric dynamics, 305 constrained by flux boundary conditions for both H<sub>2</sub> and CH<sub>4</sub>. Comparing the EMAC model output with observational data at 56 stations from the NOAA GML Carbon Cycle Cooperative Global Air Sampling Network generally indicates very good agreement at global scale. Excellent results are achieved at observational stations that experience well-mixed unpolluted air masses, suggesting that atmospheric source, sink and transport processes are accurately represented, while model performance is degraded at stations impacted by nearby pollution sources. Our H<sub>2</sub> budget is also in good agreement with bottom-up estimates 310 in the literature. We find that the EMAC model simulates the CH<sub>4</sub> chemical lifetime in excellent agreement with observational

estimates, which suggests the model calculates OH radical mixing ratios in a representative manner. The H<sub>2</sub> soil sink, based on a two-layer soil model (Yonemura et al., 2000; Ehhalt and Rohrer, 2013a; Paulot et al., 2021), in combination with monthly ERA5 reanalysis data for soil related parameters has been successfully used by the EMAC model. We conclude that atmosphere chemistry models with such features, capturing the most dominant terms of the atmospheric H<sub>2</sub> budget, should be able to  
315 generally simulate station observations of atmospheric hydrogen. This gives confidence that scenario simulations regarding the future H<sub>2</sub> economy will provide reliable estimates of its atmospheric impact.

*Code and data availability.* The Modular Earth Submodel System (MESSy) is in continuous development and is used by a consortium of institutions. Source code access and usage is licensed to all affiliates of institutions which are members of the MESSy Consortium. Institutions can become a member of the MESSy Consortium by signing the MESSy Memorandum of Understanding. The MESSy Consortium website (<http://www.messy-interface.org>) provides further information regarding access to the model. The exact version of the EMAC v2.55.2 source code and simulation set-ups used to produce the results used in this paper is archived on the Zenodo repository at  
320 <https://doi.org/10.5281/zenodo.15211346> (The MESSy Consortium, 2025).

Regarding data availability, access to the NOAA GML Carbon Cycle Cooperative Global Air Sampling Network data is available at  
325 <https://doi.org/10.15138/WP0W-EZ08> (Petron et al., 2024), the ERA5 reanalysis data is available at <https://doi.org/10.24381/cds.adbb2d47> (Hersbach et al., 2023), and the Global Fire Emissions Database (GFED) v4.1 data is available at <https://doi.org/10.3334/ORNLDAA/1293> (Randerson et al., 2017).

## **Appendix A: List of observational stations**

**Table A1.** Observational Stations from the NOAA GML Carbon Cycle Cooperative Global Air Sampling Network.

Station code	Station Name	Latitude	Longitude	Elevation (masl)	Country	Cooperating Agencies
ALT	Alert, Nunavut	82.4508° North	62.5072° West	185	Canada	Environment Canada
AMY	Anmyeon-do	36.5389° North	126.3295° East	47	Republic of Korea	Korea Global Atmosphere Watch Center, Korea Meteorological Administration
ASC	Ascension Island	7.9667° South	14.4° West	85	United Kingdom	Met Office (United Kingdom)
ASK	Assekrem	23.2625° North	5.6322° East	2710	Algeria	Office National de la Meteorologie
AZR	Terceira Island, Azores	38.766° North	27.375° West	19	Portugal	Instituto Nacional de Meteorologia e Geofisica
BHD	Baring Head Station	41.4083° South	174.871° East	85	New Zealand	National Institute of Water and Atmospheric Research
BKT	Bukit Kotabang	0.202° South	100.318° East	845	Indonesia	Bureau of Meteorology and Geophysics
BMW	Tudor Hill, Bermuda	32.2647° North	64.8788° West	30	United Kingdom	Bermuda Institute of Ocean Sciences
BRW	Barrow Atmospheric Baseline Observatory	71.323° North	156.6114° West	11	United States	NOAA Global Monitoring Laboratory
CBA	Cold Bay, Alaska	55.21° North	162.72° West	21.34	United States	U.S. National Weather Service
CGO	Cape Grim, Tasmania	40.683° South	144.69° East	94	Australia	CSIRO
CHR	Christmas Island	1.7° North	157.1518° West	0	Republic of Kiribati	Dive Kiribati
CIB	Centro de Investigacion de la Baja Atmosfera (CIBA)	41.81° North	4.93° West	845	Spain	Centro de Investigacion de la Baja Atmosfera, University of Valladolid
CPT	Cape Point	34.3523° South	18.4891° East	230	South Africa	South African Weather Service
CRZ	Crozet Island	46.4337° South	51.8478° East	197	France	Centre des Faibles Radioactivities/TAAF
DSI	Dongsha Island	20.6992° North	116.7297° East	3	Taiwan	National Central University, Taiwan
EIC	Easter Island	27.1597° South	109.4284° West	47	Chile	Direccion Meteorologica de Chile
GMI	Mariana Islands	13.386° North	144.656° East	0	Guam	University of Guam/Marina Laboratory
HBA	Halley Station, Antarctica	75.55° South	25.63° West	30	United Kingdom	British Antarctic Survey
HPB	Hohenpeissenberg	47.8011° North	11.0245° East	985	Germany	Deutscher Wetterdienst
HUN	Hegyhatal	46.9559° North	16.6521° East	248	Hungary	Institute for Nuclear Research, Hungarian Academy of Sciences
ICE	Storhofdi, Vestmannaeyjar	63.3998° North	20.2884° West	118	Iceland	Icelandic Meteorological Office
IZO	Izana, Tenerife, Canary Islands	28.309° North	16.499° West	2372.9	Spain	Izana Observatory/Meteorological State Agency of Spain
KEY	Key Biscayne, Florida	25.6654° North	80.158° West	1	United States	NOAA Atlantic Oceanographic and Meteorological Laboratory
KUM	Cape Kumukahi, Hawaii	19.5608° North	154.8883° West	8	United States	NOAA Global Monitoring Laboratory
LLN	Lulin	23.47° North	120.87° East	2862	Taiwan	Lulin Atmospheric Background Station
LMP	Lampedusa	35.5181° North	12.6322° East	45	Italy	Ente per le Nuove tecnologie, l'Energia e l'Ambiente
MEX	High Altitude Global Climate Observation Center	18.9841° North	97.311° West	4464	Mexico	Sistema International de Monitoreo Ambiental
MHD	Mace Head, County Galway	53.326° North	9.899° West	5	Ireland	National University of Ireland, Galway
MID	Sand Island, Midway	28.2186° North	177.3678° West	4.6	United States	U.S. Fish and Wildlife Service
MLO	Mauna Loa, Hawaii	19.5362° North	155.5763° West	3397	United States	NOAA Global Monitoring Laboratory
NAT	Farol De Mae Luiza Lighthouse	5.7952° South	35.1853° West	50	Brazil	Instituto de Pesquisas Energeticas e Nucleares, II Centrode Quimica e Meio Ambiente, Divisao de Quimica Ambiental
NMB	Gobabeb	23.58° South	15.03° East	456	Namibia	Gobabeb Training and Research Center
NWR	Niwot Ridge, Colorado	40.0531° North	105.5864° West	3523	United States	University of Colorado/INSTAAR
OXK	Ochsenkopf	50.3031° North	11.8084° East	1022	Germany	Max Planck Institute for Biogeochemistry
PAL	Pallas-Sammaltunturi, GAW Station	67.9733° North	24.1157° East	565	Finland	Finnish Meteorological Institute
PSA	Palmer Station, Antarctica	64.7742° South	64.0527° West	10	United States	National Science Foundation
RPB	Ragged Point	13.165° North	59.432° West	15	Barbados	Private Party
SDZ	Shangdianzi	40.65° North	117.117° East	293	China	Chinese Academy of Meteorological Sciences (CAMS) and Beijing Meteorological Bureau (BMB), China Meteorological Administration (CMA)
SEY	Mahe Island	4.6824° South	55.5325° East	2	Seychelles	Seychelles Bureau of Standards
SGP	Southern Great Plains, Oklahoma	36.607° North	97.489° West	314	United States	Lawrence Berkeley National Laboratory
SHM	Shemya Island, Alaska	52.7112° North	174.126° East	23	United States	Chugach McKinley
SMO	Tutuila	14.2474° South	170.5644° West	42	American Samoa	NOAA Global Monitoring Laboratory
SPO	South Pole, Antarctica	89.98° South	24.8° West	2810	United States	National Science Foundation
SUM	Summit	72.5962° North	38.422° West	3209.54	Greenland	National Science Foundation
SYO	Syowa Station, Antarctica	69.0125° South	39.59° East	14	Japan	Office of Polar Programs
TAP	Tae-ahn Peninsula	36.7376° North	126.1328° East	16	Republic of Korea	National Institute of Polar Research
THD	Trinidad Head, California	41.0541° North	124.151° West	107	United States	Korea Centre for Atmospheric Environment Research
TIK	Hydrometeorological Observatory of Tiksi	71.5965° North	128.8887° East	19	Russia	Scientific Aviation, Inc., NOAA Global Monitoring Laboratory, AGAGE, Scripps Institution of Oceanography, Humboldt State University Marine Laboratory
TPI	Taiping Island	10.3786° North	114.3711° East	4	Taiwan	
USH	Ushuaia	54.8484° South	68.3106° West	12	Argentina	Servicio Meteorologico Nacional
UTA	Wendover, Utah	39.9018° North	113.7181° West	1327	United States	Beth Anderson/ NWS Cooperative Observer
UUM	Ulaan Uul	44.4516° North	111.0956° East	1007	Mongolia	Mongolian Hydrometeorological Research Institute
WIS	Weizmann Institute of Science at the Arava Institute, Katura	29.9646° North	35.0605° East	151	Israel	Weizmann Institute of Science and Arava Institute for Environmental Studies
WLG	Mt. Waliguan	36.2879° North	100.8964° East	3810	Peoples Republic of China	Chinese Academy of Meteorological Sciences (CAMS) and Qinghai Meteorological Bureau (QMB), China Meteorological Administration (CMA)
ZEP	Ny-Alesund, Svalbard	78.9067° North	11.8883° East	474	Norway and Sweden	Zeppelin Station/University of Stockholm Meteorological Institute

## **Appendix B: Additional results**

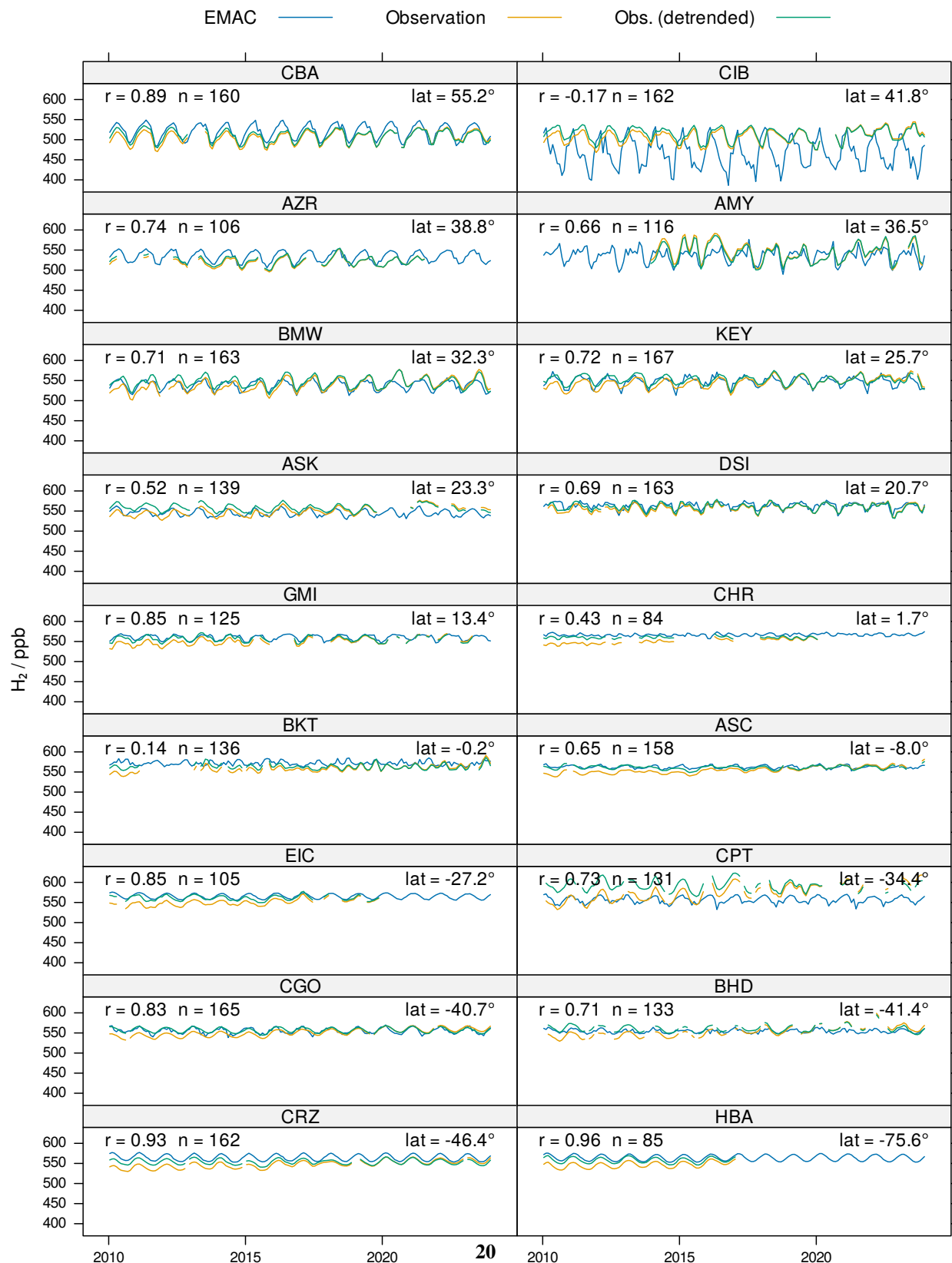


**Figure B1.** Time series comparison of observational and EMAC model data for H<sub>2</sub>. Latitudes are denoted by lat. [Other stations part 1]

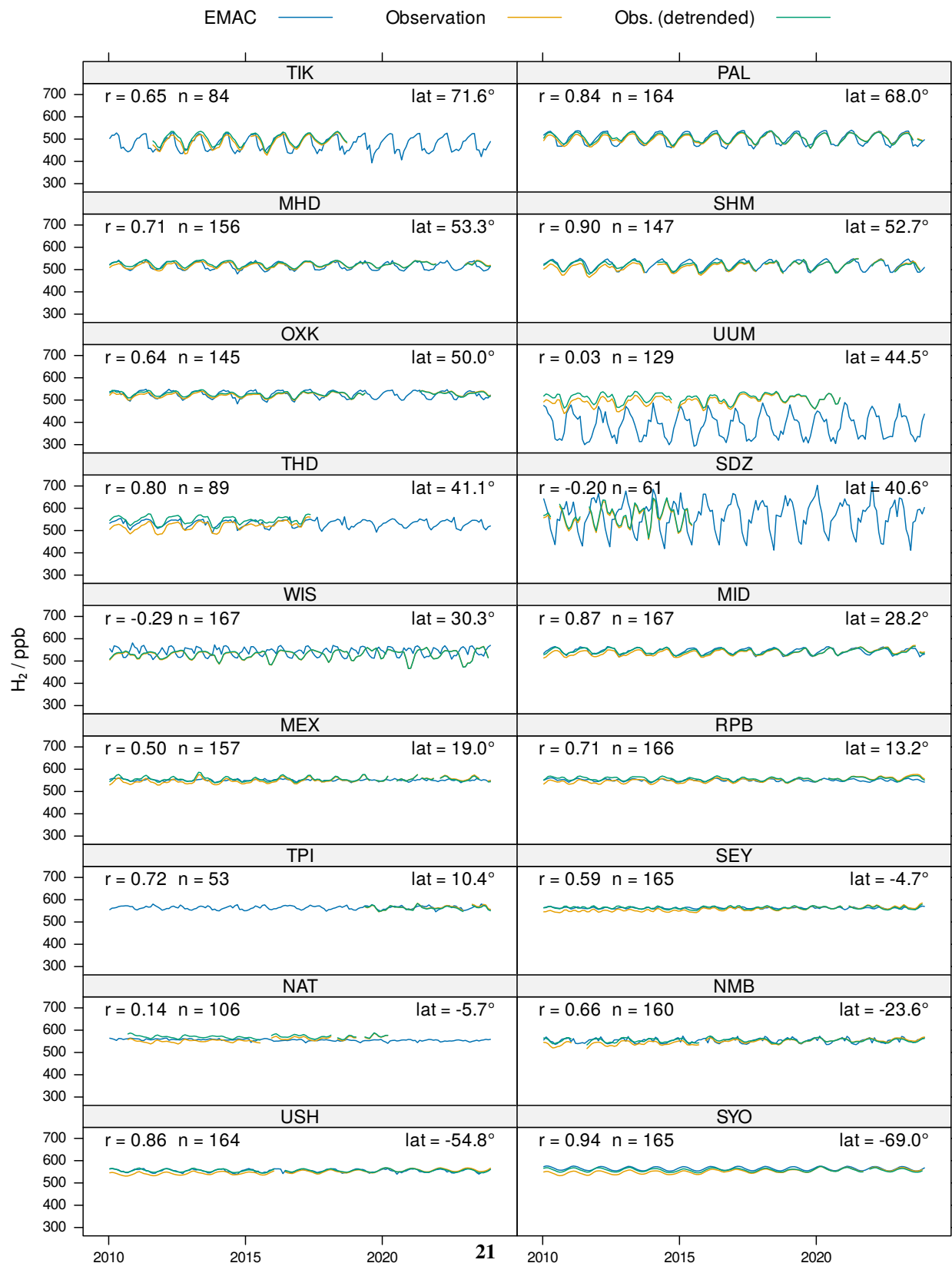


**Figure B2.** Time series comparison of observational and EMAC model data for  $H_2$ . Latitudes are denoted by lat. [Other stations part 2]

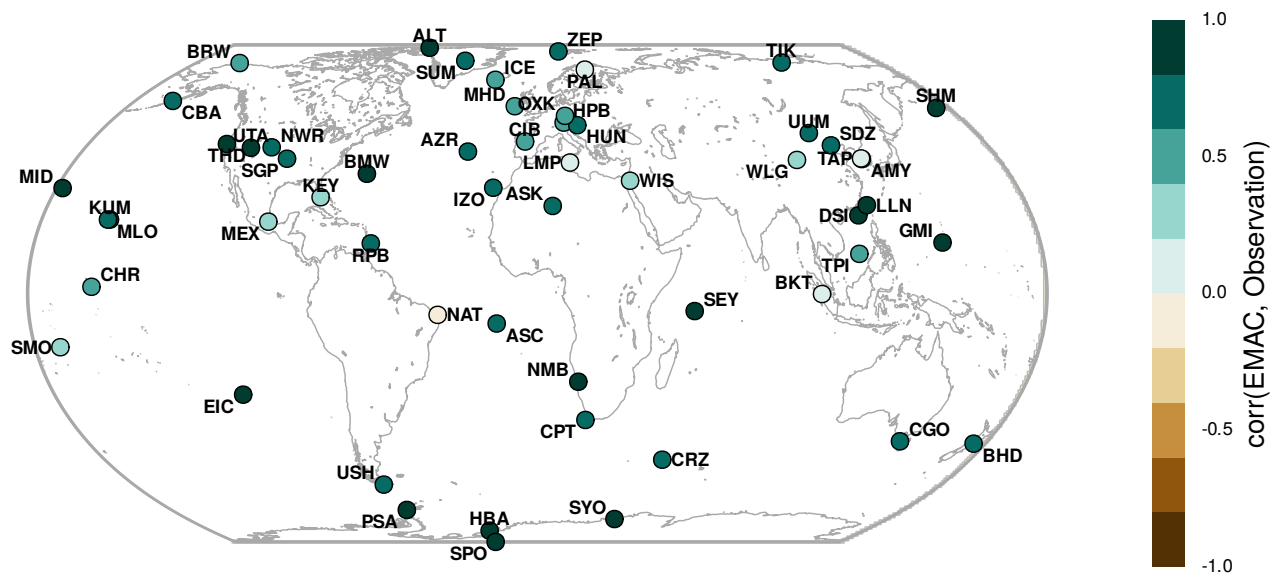


**Figure B3.** Pearson correlation coefficient between EMAC CH<sub>4</sub> mixing ratios and observational data. Model data is compared with detrended observational data for the years 2010–2023 (inclusive) to perform this calculations. For a more extensive comparison see Zimmermann et al. (2020).

**Table B1.** Comparison of mean model and observational H<sub>2</sub> mixing ratios.  $\Delta$  = Model – Observed, while  $r$  denotes the Pearson correlation coefficient. In the case of the BKT station, the EMAC value of one grid cell to the west of the station is used as it is considered more representative.

Station	Longitude	Latitude	# values	H <sub>2</sub> EMAC (ppb)	H <sub>2</sub> Observed (ppb)	$\Delta$ (ppb)	$r$
ALT	-62.5	82.5	168	504.	501.	3.19	0.93
ZEP	11.9	78.9	168	515.	513.	1.87	0.94
SUM	-38.4	72.6	168	522.	526.	-4.00	0.81
TIK	129.	71.6	84	479.	499.	-19.8	0.65
BRW	-157.	71.3	168	502.	507.	-4.82	0.81
PAL	24.1	68.0	164	503.	506.	-3.01	0.84
ICE	-20.3	63.4	168	518.	522.	-3.95	0.86
CBA	-163.	55.2	160	520.	510.	9.96	0.89
MHD	-9.90	53.3	156	517.	525.	-8.03	0.71
SHM	174.	52.7	147	521.	518.	2.89	0.90
OXK	11.8	50.0	145	525.	528.	-3.19	0.64
HPB	11.0	47.8	168	526.	527.	-1.10	0.56
HUN	16.7	47.0	168	513.	523.	-9.78	0.39
UUM	111.	44.5	129	388.	508.	-121.	0.034
CIB	-4.93	41.8	162	467.	514.	-46.9	-0.17
THD	-124.	41.1	89	532.	547.	-15.0	0.80
SDZ	117.	40.6	61	566.	569.	-2.98	-0.20
NWR	-106.	40.1	168	547.	536.	11.2	0.59
UTA	-114.	39.9	168	527.	514.	12.8	0.82
AZR	-27.4	38.8	106	533.	523.	10.4	0.74
TAP	126.	36.7	168	535.	547.	-12.7	0.62
SGP	-97.5	36.6	168	507.	519.	-12.2	0.77
AMY	126.	36.5	116	536.	543.	-7.17	0.66
WLG	101.	36.3	168	527.	529.	-1.29	0.56
LMP	12.6	35.5	168	517.	532.	-14.5	0.046
BMW	-64.9	32.3	163	539.	546.	-7.09	0.71
WIS	35.0	30.3	167	544.	530.	13.8	-0.29
IZO	-16.5	28.3	168	545.	551.	-6.18	0.61
MID	-177.	28.2	167	544.	543.	0.830	0.87
KEY	-80.2	25.7	167	548.	552.	-3.73	0.72
LLN	121.	23.5	168	563.	565.	-1.83	0.63
ASK	5.63	23.3	139	545.	558.	-13.1	0.52
DSI	117.	20.7	163	563.	560.	2.75	0.69
KUM	-155.	19.6	168	544.	544.	0.133	0.75
MLO	-156.	19.5	168	558.	548.	10.4	0.70
MEX	-97.3	19.0	157	551.	556.	-5.06	0.50
GMI	145.	13.4	125	560.	557.	3.36	0.85
RPB	-59.4	13.2	166	550.	557.	-6.91	0.71
TPI	114.	10.4	53	565.	563.	1.58	0.72
CHR	-157.	1.70	84	567.	560.	7.12	0.43
BKT	100.	-0.202	136	572.	563.	8.29	0.14
SEY	55.5	-4.68	165	563.	564.	-1.10	0.59
NAT	-35.2	-5.68	106	554.	570.	-16.9	0.14
ASC	-14.4	-7.97	158	562.	561.	1.26	0.65
SMO	-171.	-14.2	168	567.	561.	5.54	0.65
NMB	15.0	-23.6	160	554.	554.	0.158	0.66
EIC	-109.	-27.2	105	565.	561.	4.23	0.85
CPT	18.5	-34.4	131	557.	593.	-35.8	0.73
CGO	145.	-40.7	165	555.	557.	-1.56	0.83
BHD	175.	-41.4	133	554.	561.	-6.38	0.71
CRZ	51.8	-46.4	162	564.	554.	10.3	0.93
USH	-68.3	-54.8	164	554.	556.	-1.20	0.86
PSA	-64.1	-64.8	168	564.	557.	6.43	0.95
SYO	39.6	-69.0	165	564.	558.	6.05	0.94
HBA	-26.2	-75.6	85	564.	558.	5.79	0.96
SPO	-24.8	-89.5	168	564.	558.	5.81	0.96

330 *Author contributions.* JL managed the project with contributions from AP. BS led the delivery of model simulations with contributions from AP, KK, SG, CB and NS. KK led the delivery of soil sink modelling with contributions from BS. CB led the collation of observational data and its quality control with contributions from BS. SG led the delivery of chemical tagging with contributions from BS. NS wrote the manuscript with contributions from all co-authors. All authors met to discuss the results and contributed to the writing and editing of the manuscript.

335 *Competing interests.* We declare that two of the co-authors hold an editorial board position with Geoscientific Model Development. The authors have no other competing interests to declare.

### **Acknowledgements**

N. S. acknowledges funding support from the CSIRO International Hydrogen Research Fellowship scheme and the Faculty of Engineering and Information Technology at UTS to undertake a sabbatical at the Max Planck Institute for Chemistry in Mainz. All simulations were performed with the Levante High Performance Computing System (<https://www.dkrz.de/en/systems/hpc/hlre-4-levante>) hosted by Deutsches Klimarechenzentrum GmbH.

## References

Akagi, S. K., Yokelson, R. J., Wiedinmyer, C., Alvarado, M. J., Reid, J. S., Karl, T., Crounse, J. D., and Wennberg, P. O.: Emission factors for open and domestic biomass burning for use in atmospheric models, *Atmospheric Chemistry and Physics*, 11, 4039–4072, <https://doi.org/10.5194/acp-11-4039-2011>, 2011.

345 Andreae, M. O.: Emission of trace gases and aerosols from biomass burning—an updated assessment, *Atmospheric Chemistry and Physics*, 19, 8523–8546, <https://doi.org/10.5194/acp-19-8523-2019>, 2019.

Archibald, A. T., Levine, J. G., Abraham, N. L., Cooke, M. C., Edwards, P. M., Heard, D. E., Jenkin, M. E., Karunaharan, A., Pike, R. C., Monks, P. S., Shallcross, D. E., Telford, P. J., Whalley, L. K., and Pyle, J. A.: Impacts of HO<sub>x</sub> regeneration and recycling in the oxidation of isoprene: Consequences for the composition of past, present and future atmospheres, *Geophysical Research Letters*, 38, L05 804, 350 <https://doi.org/10.1029/2010gl046520>, 2011.

Bourtsoukidis, E., Pozzer, A., Sattler, T., Matthaios, V. N., Ernle, L., Edtbauer, A., Fischer, H., Könemann, T., Osipov, S., Paris, J.-D., Pfannerstill, E. Y., Stönnér, C., Tadic, I., Walter, D., Wang, N., Lelieveld, J., and Williams, J.: The Red Sea Deep Water is a potent source of atmospheric ethane and propane, *Nature Communications*, 11, 447, <https://doi.org/10.1038/s41467-020-14375-0>, 2020.

Brasseur, G. P., Kiehl, J. T., Müller, J.-F., Schneider, T., Granier, C., Tie, X. X., and Hauglustaine, D.: Past and future changes in global 355 tropospheric ozone: Impact on radiative forcing, *Geophysical Research Letters*, 25, 3807–3810, <https://doi.org/10.1029/1998gl900013>, 1998.

Brenninkmeijer, C. A. M., Crutzen, P., Boumard, F., Dauer, T., Dix, B., Ebinghaus, R., Filippi, D., Fischer, H., Franke, H., Frieß, U., Heintzenberg, J., Helleis, F., Hermann, M., Kock, H. H., Koeppel, C., Lelieveld, J., Leuenberger, M., Martinsson, B. G., Miemczyk, S., Moret, H. P., Nguyen, H. N., Nyfeler, P., Oram, D., O’Sullivan, D., Penkett, S., Platt, U., Pupek, M., Ramonet, M., Randa, B., Reichelt, M., 360 Rhee, T. S., Rohwer, J., Rosenfeld, K., Scharffe, D., Schlager, H., Schumann, U., Slemr, F., Sprung, D., Stock, P., Thaler, R., Valentino, F., van Velthoven, P., Waibel, A., Wandel, A., Waschitschek, K., Wiedensohler, A., Xueref-Remy, I., Zahn, A., Zech, U., and Ziereis, H.: Civil Aircraft for the regular investigation of the atmosphere based on an instrumented container: The new CARIBIC system, *Atmospheric Chemistry and Physics*, 7, 4953–4976, <https://doi.org/10.5194/acp-7-4953-2007>, 2007.

Collins, W. J., Lamarque, J.-F., Schulz, M., Boucher, O., Eyring, V., Hegglin, M. I., Maycock, A., Myhre, G., Prather, M., Shindell, D., and 365 Smith, S. J.: AerChemMIP: quantifying the effects of chemistry and aerosols in CMIP6, *Geoscientific Model Development*, 10, 585–607, <https://doi.org/10.5194/gmd-10-585-2017>, 2017.

Derwent, R., Simmonds, P., O’Doherty, S., Manning, A., Collins, W., and Stevenson, D.: Global environmental impacts of the hydrogen economy, *International Journal of Nuclear Hydrogen Production and Application*, 1, 57–67, <https://doi.org/10.1504/IJNHPA.2006.009869>, 2006.

370 Derwent, R. G., Stevenson, D. S., Utembe, S. R., Jenkin, M. E., Khan, A. H., and Shallcross, D. E.: Global modelling studies of hydrogen and its isotopomers using STOCHEM-CRI: Likely radiative forcing consequences of a future hydrogen economy, *International Journal of Hydrogen Energy*, 45, 9211–9221, <https://doi.org/10.1016/j.ijhydene.2020.01.125>, 2020.

Ehhalt, D. H. and Rohrer, F.: The tropospheric cycle of H<sub>2</sub>: a critical review, *Tellus B: Chemical and Physical Meteorology*, 61B, 500—535, <https://doi.org/10.1111/j.1600-0889.2009.00416.x>, 2009.

375 Ehhalt, D. H. and Rohrer, F.: The dependence of soil H<sub>2</sub> uptake on temperature and moisture: a reanalysis of laboratory data, *Tellus B: Chemical and Physical Meteorology*, 63B, 1040—1051, <https://doi.org/10.1111/j.1600-0889.2011.00581.x>, 2011.

Ehhalt, D. H. and Rohrer, F.: Deposition velocity of H<sub>2</sub>: a new algorithm for its dependence on soil moisture and temperature, *Tellus B: Chemical and Physical Meteorology*, 65, 19 904, <https://doi.org/10.3402/tellusb.v65i0.19904>, 2013a.

Ehhalt, D. H. and Rohrer, F.: Dry deposition of molecular hydrogen in the presence of H<sub>2</sub> production, *Tellus B: Chemical and Physical Meteorology*, 65, 20 620, <https://doi.org/10.3402/tellusb.v65i0.20620>, 2013b.

Ellis, G. S. and Gelman, S. E.: Model predictions of global geologic hydrogen resources, *Science Advances*, 10, eado0955, <https://doi.org/10.1126/sciadv.ado0955>, 2024.

Esquivel-Elizondo, S., Hormaza Mejia, A., Sun, T., Shrestha, E., Hamburg, S. P., and Ocko, I. B.: Wide range in estimates of hydrogen emissions from infrastructure, *Frontiers in Energy Research*, 11, 1207 208, <https://doi.org/10.3389/fenrg.2023.1207208>, 2023.

Fan, Z., Sheerazi, H., Bhardwaj, A., Corbeau, A.-S., Longobardi, K., Castañeda, A., Merz, A.-K., Woodall, C. M., Agrawal, M., Orozco-Sanchez, S., and Friedmann, J.: Hydrogen leakage: a potential risk for the hydrogen economy, The Center on Global Energy Policy at Columbia University, pp. 1-33, [https://www.energypolicy.columbia.edu/sites/default/files/file-uploads/HydrogenLeakageRegulations\\_CGEP\\_Commentary\\_063022.pdf](https://www.energypolicy.columbia.edu/sites/default/files/file-uploads/HydrogenLeakageRegulations_CGEP_Commentary_063022.pdf) (last access: 6 Septemer 2024), 2022.

Galimova, T., Ram, M., and Breyer, C.: Mitigation of air pollution and corresponding impacts during a global energy transition towards 100% renewable energy system by 2050, *Energy Reports*, 8, 14 124–14 143, <https://doi.org/10.1016/j.egyr.2022.10.343>, 2022.

Ganzeveld, L., Bouwman, L., Stehfest, E., van Vuuren, D. P., Eickhout, B., and Lelieveld, J.: Impact of future land use and land cover changes on atmospheric chemistry-climate interactions, *Journal of Geophysical Research: Atmospheres*, 115, D23 301, <https://doi.org/10.1029/2010jd014041>, 2010.

Giglio, L., Randerson, J. T., and van der Werf, G. R.: Analysis of daily, monthly, and annual burned area using the fourth-generation global fire emissions database (GFED4), *Journal of Geophysical Research: Biogeosciences*, 118, 317–328, <https://doi.org/10.1002/jgrg.20042>, 2013.

GLDAS: GLDAS Soil Land Surface, <https://ldas.gsfc.nasa.gov/gldas/soils>, (last access: 24 September 2024), 2024.

Granier, C., Darras, S., Denier van der Gon, H., Doubalova, J., Elguindi, N., Galle, B., Gauss, M., Guevara, M., Jalkanen, J.-P., Kuenen, J., Liouesse, C., Quack, B., Simpson, D., and Sindelarova, K.: The Copernicus Atmosphere Monitoring Service global and regional emissions (April 2019 version), Copernicus Atmosphere Monitoring Service (CAMS) report, pp. 1–54, <https://doi.org/10.24380/d0bn-kx16>, 2019.

Guenther, A., Hewitt, C. N., Erickson, D., Fall, R., Geron, C., Graedel, T., Harley, P., Klinger, L., Lerdau, M., McKay, W. A., Pierce, T., Scholes, B., Steinbrecher, R., Tallamraju, R., Taylor, J., and Zimmerman, P.: A global model of natural volatile organic compound emissions, *Journal of Geophysical Research: Atmospheres*, 100, 8873–8892, <https://doi.org/10.1029/94JD02950>, 1995.

Hand, E.: Hidden Hydrogen. Does Earth hold vast stores of a renewable carbon-free fuel?, *Science*, 379, 630–636, <https://doi.org/10.1126/science.adh1460>, 2023.

Hauglustaine, D. A. and Ehhalt, D. H.: A three-dimensional model of molecular hydrogen in the troposphere, *Journal of Geophysical Research: Atmospheres*, 107, 4330, <https://doi.org/10.1029/2001JD001156>, 2002.

Hersbach, H., Bell, B., Berrisford, P., Hirahara, S., Horányi, A., Muñoz-Sabater, J., Nicolas, J., Peubey, C., Radu, R., Schepers, D., Simmons, A., Soci, C., Abdalla, S., Abellán, X., Balsamo, G., Bechtold, P., Biavati, G., Bidlot, J., Bonavita, M., De Chiara, G., Dahlgren, P., Dee, D., Diamantakis, M., Dragani, R., Flemming, J., Forbes, R., Fuentes, M., Geer, A., Haimberger, L., Healy, S., Hogan, R. J., Hólm, E., Janisková, M., Keeley, S., Laloyaux, P., Lopez, P., Lupu, C., Radnoti, G., de Rosnay, P., Rozum, I., Vamborg, F., Vil- laume, S., and Thépaut, J.-N.: The ERA5 global reanalysis, *Quarterly Journal of the Royal Meteorological Society*, 146, 1999–2049, <https://doi.org/10.1002/qj.3803>, 2020.

Hersbach, H., Bell, B., Berrisford, P., Biavati, G., Horányi, A., Muñoz Sabater, J., Nicolas, J., Peubey, C., Radu, R., Rozum, I., Schepers, D.,  
415 Simmons, A., Soci, C., Dee, D., and Thépaut, J.-N.: ERA5 hourly data on single levels from 1940 to present, Copernicus Climate Change Service (C3S) Climate Data Store (CDS) (last access: 19 September 2024), <https://doi.org/10.24381/cds.adbb2d47>, 2023.

Houweling, S., Kaminski, T., Dentener, F., Lelieveld, J., and Heimann, M.: Inverse modeling of methane sources and sinks using the adjoint of a global transport model, *Journal of Geophysical Research: Atmospheres*, 104, 26 137–26 160, <https://doi.org/10.1029/1999JD900428>, 1999.

420 Hydrogen Council: Hydrogen for Net-Zero. A critical cost-competitive energy vector, pp. 1-56, <https://hydrogencouncil.com/en/hydrogen-for-net-zero/> (last access: 6 September 2024), 2021.

International Energy Agency: Energy Technology Perspectives 2020. Special Report on Carbon Capture Utilisation and Storage: CCUS in clean energy transitions., pp. 1-174, [https://www.oecd-ilibrary.org/energy/energy-technology-perspectives-2020-special-report-on-carbon-capture-utilisation-and-storage\\_208b66f4-en](https://www.oecd-ilibrary.org/energy/energy-technology-perspectives-2020-special-report-on-carbon-capture-utilisation-and-storage_208b66f4-en) (last access: 6 September 2024), 2020.

425 International Energy Agency: Global Hydrogen Review 2023, pp. 1-176, <https://www.iea.org/reports/global-hydrogen-review-2023> (last access: 6 September 2024), 2023.

Jöckel, P., Tost, H., Pozzer, A., Brühl, C., Buchholz, J., Ganzeveld, L., Hoor, P., Kerkweg, A., Lawrence, M. G., Sander, R., Steil, B.,  
430 Stiller, G., Tanarhte, M., Taraborrelli, D., van Aardenne, J., and Lelieveld, J.: The atmospheric chemistry general circulation model ECHAM5/MESSy1: consistent simulation of ozone from the surface to the mesosphere, *Atmospheric Chemistry and Physics*, 6, 5067–5104, <https://doi.org/10.5194/acp-6-5067-2006>, 2006.

Jöckel, P., Kerkweg, A., Pozzer, A., Sander, R., Tost, H., Riede, H., Baumgaertner, A., Gromov, S., and Kern, B.: Development cycle 2 of the Modular Earth Submodel System (MESSy2), *Geoscientific Model Development*, 3, 717–752, <https://doi.org/10.5194/gmd-3-717-2010>, 2010.

435 Kaiser, J. W., Heil, A., Andreae, M. O., Benedetti, A., Chubarova, N., Jones, L., Morcrette, J.-J., Razinger, M., Schultz, M. G., Suttie, M., and van der Werf, G. R.: Biomass burning emissions estimated with a global fire assimilation system based on observed fire radiative power, *Biogeosciences*, 9, 527–554, <https://doi.org/10.5194/bg-9-527-2012>, 2012.

Kerkweg, A., Sander, R., Tost, H., and Jöckel, P.: Technical note: Implementation of prescribed (OFFLEM), calculated (ONLEM), and pseudo-emissions (TNUUDGE) of chemical species in the Modular Earth Submodel System (MESSy), *Atmospheric Chemistry and Physics*, 6, 3603–3609, <https://doi.org/10.5194/acp-6-3603-2006>, 2006.

440 Lan, X., Thoning, K., and Dlugokencky, E.: Trends in globally-averaged CH<sub>4</sub>, N<sub>2</sub>O, and SF<sub>6</sub> determined from NOAA Global Monitoring Laboratory measurements, <https://doi.org/https://doi.org/10.15138/P8XG-AA10>, 2024.

Lelieveld, J., Gromov, S., Pozzer, A., and Taraborrelli, D.: Global tropospheric hydroxyl distribution, budget and reactivity, *Atmospheric Chemistry and Physics*, 16, 12 477–12 493, <https://doi.org/10.5194/acp-16-12477-2016>, 2016.

Martin, A., Gayler, V., Steil, B., Klingmüller, K., Jöckel, P., Tost, H., Lelieveld, J., and Pozzer, A.: Evaluation of the coupling of EMACv2.55  
445 to the land surface and vegetation model JSBACHv4, *Geoscientific Model Development*, 17, 5705–5732, <https://doi.org/10.5194/gmd-17-5705-2024>, 2024.

Millington, R. J. and Quirk, J. P.: Permeability of Porous Media, *Nature*, 183, 387–388, <https://doi.org/10.1038/183387a0>, 1959.

Nicely, J. M., Duncan, B. N., Hanisco, T. F., Wolfe, G. M., Salawitch, R. J., Deushi, M., Haslerud, A. S., Jöckel, P., Josse, B., Kinnison, D. E., Klekociuk, A., Manyin, M. E., Marécal, V., Morgenstern, O., Murray, L. T., Myhre, G., Oman, L. D., Pitari, G., Pozzer, A., Quaglia, I., Revell, L. E., Rozanov, E., Stenke, A., Stone, K., Strahan, S., Tilmes, S., Tost, H., Westervelt, D. M., and Zeng, G.: A machine learning

examination of hydroxyl radical differences among model simulations for CCM1-1, *Atmospheric Chemistry and Physics*, 20, 1341–1361, <https://doi.org/10.5194/acp-20-1341-2020>, 2020.

Novelli, P. C., Lang, P. M., Masarie, K. A., Hurst, D. F., Myers, R., and Elkins, J. W.: Molecular hydrogen in the troposphere: Global distribution and budget, *Journal of Geophysical Research: Atmospheres*, 104, 30 427–30 444, <https://doi.org/10.1029/1999JD900788>, 1999.

Ocko, I. B. and Hamburg, S. P.: Climate consequences of hydrogen emissions, *Atmospheric Chemistry and Physics*, 22, 9349–9368, <https://doi.org/10.5194/acp-22-9349-2022>, 2022.

Paulot, F., Paynter, D., Naik, V., Malyshev, S., Menzel, R., and Horowitz, L. W.: Global modeling of hydrogen using GFDL-AM4.1: Sensitivity of soil removal and radiative forcing, *International Journal of Hydrogen Energy*, 46, 13 446–13 460, <https://doi.org/10.1016/j.ijhydene.2021.01.088>, 2021.

460 Paulot, F., Pétron, G., Crotwell, A. M., and Bertagni, M. B.: Reanalysis of NOAA H<sub>2</sub> observations: implications for the H<sub>2</sub> budget, *Atmospheric Chemistry and Physics*, 24, 4217–4229, <https://doi.org/10.5194/acp-24-4217-2024>, 2024.

Petron, G., Crotwell, A. M., Madronich, M., Moglia, E., Baugh, K. E., Kitzis, D., Mefford, T., DeVogel, S., Neff, D., Lan, X., Crotwell, M. J., Thoning, K., Wolter, S., and Mund, J. W.: Atmospheric Hydrogen Dry Air Mole Fractions from the NOAA GML Carbon Cycle 465 Cooperative Global Air Sampling Network, 2009–2023 Version: 2024-07-30, <https://doi.org/10.15138/WP0W-EZ08>, 2024.

Pieterse, G., Krol, M. C., Batenburg, A. M., Steele, L. P., Krummel, P. B., Langenfelds, R. L., and Röckmann, T.: Global modelling of H<sub>2</sub> mixing ratios and isotopic compositions with the TM5 model, *Atmospheric Chemistry and Physics*, 11, 7001–7026, <https://doi.org/10.5194/acp-11-7001-2011>, 2011.

470 Plummer, D., Nagashima, T., Tilmes, S., Archibald, A., Chiodo, G., Fadnavis, S., Garny, H., Josse, B., Kim, J., Lamarque, J.-F., Morgenstern, O., Murray, L., Orbe, C., Tai, A., Chipperfield, M., Funke, B., Juckes, M., Kinnison, D., Kunze, M., Luo, B., Matthes, K., Newman, P. A., Pascoe, C., and Peter, T.: CCM1-2022: a new set of Chemistry–Climate Model Initiative (CCMI) community simulations to update the assessment of models and support upcoming ozone assessment activities, *SPARC Newsletter*, [https://www.aparc-climate.org/wp-content/uploads/2021/07/SPARCnewsletter\\_Jul2021\\_web.pdf](https://www.aparc-climate.org/wp-content/uploads/2021/07/SPARCnewsletter_Jul2021_web.pdf) (last access: 13 September 2025), 57, 22–30, 2021.

Pöschl, U., von Kuhlmann, R., Poisson, N., and Crutzen, P. J.: Development and intercomparison of condensed isoprene oxidation mechanisms for global atmospheric modeling, *Journal of Atmospheric Chemistry*, 37, 29–52, <https://doi.org/10.1023/A:1006391009798>, 2000.

475 Prather, M. J. and Zhu, L.: Resetting tropospheric OH and CH<sub>4</sub> lifetime with ultraviolet H<sub>2</sub>O absorption, *Science*, 385, 201–204, <https://doi.org/10.1126/science.adn0415>, 2024.

Prather, M. J., Holmes, C. D., and Hsu, J.: Reactive greenhouse gas scenarios: Systematic exploration of uncertainties and the role of atmospheric chemistry, *Geophysical Research Letters*, 39, 1–5, <https://doi.org/10.1029/2012GL051440>, 2012.

480 Price, H., Jaeglé, L., Rice, A., Quay, P., Novelli, P. C., and Gammon, R.: Global budget of molecular hydrogen and its deuterium content: Constraints from ground station, cruise, and aircraft observations, *Journal of Geophysical Research: Atmospheres*, 112, D22 108, <https://doi.org/10.1029/2006JD008152>, 2007.

Randerson, J. T., van der Werf, G. R., Giglio, L., Collatz, G. J., and Kasibhatla, P. S.: Global fire emissions database, version 4.1 (GFEDv4), ORNL DAAC, Oak Ridge, Tennessee, USA. [https://daac.ornl.gov/cgi-bin/dsviewer.pl?ds\\_id=1293](https://daac.ornl.gov/cgi-bin/dsviewer.pl?ds_id=1293) (last access: 22 December 2024), <https://doi.org/10.3334/ORNLDaac/1293>, 2017.

485 Reifenberg, S. F., Martin, A., Kohl, M., Bacer, S., Hamryszczak, Z., Tadic, I., Röder, L., Crowley, D. J., Fischer, H., Kaiser, K., Schneider, J., Dörich, R., Crowley, J. N., Tomsche, L., Marsing, A., Voigt, C., Zahn, A., Pöhlker, C., Holanda, B. A., Krüger, O., Pöschl, U., Pöhlker, M., Jöckel, P., Dorf, M., Schumann, U., Williams, J., Bohn, B., Curtius, J., Harder, H., Schlager, H., Lelieveld, J., and Pozzer, A.: Numerical

simulation of the impact of COVID-19 lockdown on tropospheric composition and aerosol radiative forcing in Europe, *Atmospheric Chemistry and Physics*, 22, 10 901–10 917, <https://doi.org/10.5194/acp-22-10901-2022>, 2022.

Rhee, T. S., Brenninkmeijer, C. A. M., Braß, M., and Brühl, C.: Isotopic composition of H<sub>2</sub> from CH<sub>4</sub> oxidation in the stratosphere and the troposphere, *Journal of Geophysical Research: Atmospheres*, 111, D23 303, <https://doi.org/10.1029/2005JD006760>, 2006.

Righi, M., Hendricks, J., and Sausen, R.: The global impact of the transport sectors on atmospheric aerosol: simulations for year 2000 emissions, *Atmospheric Chemistry and Physics*, 13, 9939–9970, <https://doi.org/10.5194/acp-13-9939-2013>, 2013.

Rodell, M., Houser, P. R., Jambor, U., Gottschalck, J., Mitchell, K., Meng, C.-J., Arsenault, K., Cosgrove, B., Radakovich, J., Bosilovich, M., Entin, J. K., Walker, J. P., Lohmann, D., and Toll, D.: The Global Land Data Assimilation System, *Bulletin of the American Meteorological Society*, 85, 381–394, <https://doi.org/10.1175/BAMS-85-3-381>, 2004.

Roeckner, E., Bäuml, G., Bonaventura, L., Brokopf, R., Esch, M., Giorgetta, M., Hagemann, S., Kirchner, I., Kornblueh, L., Manzini, E., Rhodin, A., Schlese, U., Schulzweida, U., and Tompkins, A.: Report No 349: the atmospheric general circulation model ECHAM5, Part I., pp. 1–133, [https://pure.mpg.de/pubman/faces/ViewItemOverviewPage.jsp?itemId=item\\_995269](https://pure.mpg.de/pubman/faces/ViewItemOverviewPage.jsp?itemId=item_995269) (last access: 22 December 2024), 2003.

Roeckner, E., Brokopf, R., Esch, M., Giorgetta, M., Hagemann, S., Kornblueh, L., Manzini, E., Schlese, U., and Schulzweida, U.: Report No. 354: the atmospheric general circulation model ECHAM5, Part II., pp. 1–64, [https://pure.mpg.de/pubman/faces/ViewItemOverviewPage.jsp?itemId=item\\_995221](https://pure.mpg.de/pubman/faces/ViewItemOverviewPage.jsp?itemId=item_995221) (last access: 22 December 2024), 2004.

Roeckner, E., Brokopf, R., Esch, M., Giorgetta, M., Hagemann, S., Kornblueh, L., Manzini, E., Schlese, U., and Schulzweida, U.: Sensitivity of Simulated Climate to Horizontal and Vertical Resolution in the ECHAM5 Atmosphere Model, *Journal of Climate*, 19, 3771–3791, <https://doi.org/10.1175/JCLI3824.1>, 2006.

Sand, M., Skeie, R. B., Sandstad, M., Krishnan, S., Myhre, G., Bryant, H., Derwent, R., Hauglustaine, D., Paulot, F., Prather, M., and Stevenson, D.: A multi-model assessment of the Global Warming Potential of hydrogen, *Communications Earth & Environment*, 4, 203, <https://doi.org/10.1038/s43247-023-00857-8>, 2023.

Sanderson, M. G., Collins, W. J., Derwent, R. G., and Johnson, C. E.: Simulation of Global Hydrogen Levels Using a Lagrangian Three-Dimensional Model, *Journal of Atmospheric Chemistry*, 46, 15–28, <https://doi.org/10.1023/A:1024824223232>, 2003.

Saunois, M., Martinez, A., Poulter, B., Zhang, Z., Raymond, P. A., Regnier, P., Canadell, J. G., Jackson, R. B., Patra, P. K., Bousquet, P., Ciais, P., Dlugokencky, E. J., Lan, X., Allen, G. H., Bastviken, D., Beerling, D. J., Belikov, D. A., Blake, D. R., Castaldi, S., Crippa, M., Deemer, B. R., Dennison, F., Etiöpe, G., Gedney, N., Höglund-Isaksson, L., Holgerson, M. A., Hopcroft, P. O., Hugelius, G., Ito, A., Jain, A. K., Janardanan, R., Johnson, M. S., Kleinen, T., Krummel, P. B., Lauerwald, R., Li, T., Liu, X., McDonald, K. C., Melton, J. R., Mühle, J., Müller, J., Murguia-Flores, F., Niwa, Y., Noce, S., Pan, S., Parker, R. J., Peng, C., Ramonet, M., Riley, W. J., Rocher-Ros, G., Rosentreter, J. A., Sasakawa, M., Segers, A., Smith, S. J., Stanley, E. H., Thanwerdas, J., Tian, H., Tsuruta, A., Tubiello, F. N., Weber, T. S., van der Werf, G. R., Worthy, D. E. J., Xi, Y., Yoshida, Y., Zhang, W., Zheng, B., Zhu, Q., Zhu, Q., and Zhuang, Q.: Global Methane Budget 2000–2020, *Earth System Science Data*, 17, 1873–1958, <https://doi.org/10.5194/essd-17-1873-2025>, 2025.

Schultz, M. G., Diehl, T., Brasseur, G. P., and Zittel, W.: Air pollution and climate-forcing impacts of a global hydrogen economy, *Science*, 302, 624–627, <https://doi.org/10.1126/science.1089527>, 2003.

Schultz, M. G., Heil, A., Hoelzemann, J. J., Spessa, A., Thonicke, K., Goldammer, J. G., Held, A. C., Pereira, J. M., and van het Bolscher, M.: Global wildland fire emissions from 1960 to 2000, *Global Biogeochemical Cycles*, 22, GB2002, <https://doi.org/10.1029/2007GB003031>, 2008.

525 Seiler, W. and Conrad, R.: Dickinson, R. E. (editor). Contribution of tropical ecosystems to the global budgets of trace gases, especially CH<sub>4</sub>, H<sub>2</sub>, CO, and N<sub>2</sub>O, in: The Geophysiology of Amazonia: Vegetation and Climate Interactions, pp. 133–162, John Wiley, New York, ISBN 0471845116, 1987.

Smith-Downey, N. V., Randerson, J. T., and Eiler, J. M.: Temperature and moisture dependence of soil H<sub>2</sub> uptake measured in the laboratory, *Geophysical Research Letters*, 33, L14 813, <https://doi.org/10.1029/2006GL026749>, 2006.

530 SPARC: SPARC Report on the Lifetimes of Stratospheric Ozone-Depleting Substances, Their Replacements, and Related Species, Ko, M. and Newman, P. and Reimann, S. and Strahan, S. (editors), pp. 1-255, <https://www.aparc-climate.org/publications/sparc-reports/sparc-report-no-6/> (last access: 13 September 2025), 2013.

The MESSy Consortium: The Modular Earth Submodel System Version 2.55.2\_no-branch\_b4754874\_H2, <https://doi.org/https://doi.org/10.5281/zenodo.15211346>, 2025.

535 Tromp, T. K., Shia, R.-L., Allen, M., Eiler, J. M., and Yung, Y. L.: Potential environmental impact of a hydrogen economy on the stratosphere, *Science*, 300, 1740–1742, <https://doi.org/10.1126/science.1085169>, 2003.

Truche, L., Donzé, F.-V., Goskolli, E., Muceku, B., Loisy, C., Monnin, C., Dutoit, H., and Cerepi, A.: A deep reservoir for hydrogen drives intense degassing in the Bulqizë ophiolite, *Science*, 383, 618–621, <https://doi.org/10.1126/science.adk9099>, 2024.

540 Van Aardenne, J. A., Dentener, F. J., Olivier, J. G. J., Peters, J. A. H. W., and Ganzeveld, L. N.: The EDGAR 3.2 Fast track 2000 dataset (32FT2000), [https://www.researchgate.net/profile/Frank-Dentener/publication/233894132\\_The\\_EDGAR\\_32\\_Fast\\_track\\_2000\\_dataset\\_32FT2000/links/02e7e52fa254d80ba0000000/The-EDGAR-32-Fast-track-2000-dataset-32FT2000.pdf](https://www.researchgate.net/profile/Frank-Dentener/publication/233894132_The_EDGAR_32_Fast_track_2000_dataset_32FT2000/links/02e7e52fa254d80ba0000000/The-EDGAR-32-Fast-track-2000-dataset-32FT2000.pdf) (last access: 22 December 2024), 32, 2005.

Warneck, P.: Chemistry of the Natural Atmosphere., International Geophysics Series, Volume 41, pp. 1-757, Academic Press, San Diego, ISBN 9780080954684, 1988.

545 Warwick, N., Griffiths, P., Keeble, J., Archibald, A., Pyle, J., and Shine, K.: Atmospheric implications of increased Hydrogen use, University of Cambridge and University of Reading, pp. 1-75, <https://assets.publishing.service.gov.uk/media/624eca7fe90e0729f4400b99/atmospheric-implications-of-increased-hydrogen-use.pdf> (last access: 22 December 2024), 2022.

Warwick, N. J., Bekki, S., Nisbet, E. G., and Pyle, J. A.: Impact of a hydrogen economy on the stratosphere and troposphere studied in a 2-D model, *Geophysical Research Letters*, 31, L05 107, <https://doi.org/10.1029/2003GL019224>, 2004.

550 Warwick, N. J., Archibald, A. T., Griffiths, P. T., Keeble, J., O'Connor, F. M., Pyle, J. A., and Shine, K. P.: Atmospheric composition and climate impacts of a future hydrogen economy, *Atmospheric Chemistry and Physics*, 23, 13 451–13 467, <https://doi.org/10.5194/acp-23-13451-2023>, 2023.

Xiao, X., Prinn, R. G., Simmonds, P. G., Steele, L. P., Novelli, P. C., Huang, J., Langenfelds, R. L., O'Doherty, S., Krummel, P. B., Fraser, 555 P. J., Porter, L. W., Weiss, R. F., Salameh, P., and Wang, R. H. J.: Optimal estimation of the soil uptake rate of molecular hydrogen from the Advanced Global Atmospheric Gases Experiment and other measurements, *Journal of Geophysical Research: Atmospheres*, 112, D07 303, <https://doi.org/10.1029/2006JD007241>, 2007.

Yang, L. H., Jacob, D. J., Lin, H., Dang, R., Bates, K. H., East, J. D., Travis, K. R., Pendergrass, D. C., and Murray, L. T.: Assessment of Hydrogen's Climate Impact Is Affected by Model OH Biases, *Geophysical Research Letters*, 52, e2024GL112445, 560 <https://doi.org/10.1029/2024GL112445>, 2025.

Yashiro, H., Sudo, K., Yonemura, S., and Takigawa, M.: The impact of soil uptake on the global distribution of molecular hydrogen: chemical transport model simulation, *Atmospheric Chemistry and Physics*, 11, 6701–6719, <https://doi.org/10.5194/acp-11-6701-2011>, 2011.

Yonemura, S., Yokozawa, M., Kawashima, S., and Tsuruta, H.: Model analysis of the influence of gas diffusivity in soil on CO and H<sub>2</sub> uptake, *Tellus B: Chemical and Physical Meteorology*, 52B, 919–933, <https://doi.org/10.3402/tellusb.v52i3.17075>, 2000.

565 Zimmermann, P. H., Brenninkmeijer, C. A. M., Pozzer, A., Jöckel, P., Winterstein, F., Zahn, A., Houweling, S., and Lelieveld, J.: Model simulations of atmospheric methane (1997–2016) and their evaluation using NOAA and AGAGE surface and IAGOS-CARIBIC aircraft observations, *Atmospheric Chemistry and Physics*, 20, 5787–5809, <https://doi.org/10.5194/acp-20-5787-2020>, 2020.